nature nanotechnology

Article

https://doi.org/10.1038/s41565-023-01417-z

Berry curvature dipole generation and helicity-to-spin conversion at symmetry-mismatched heterointerfaces

In the format provided by the authors and unedited

Table-of-contents:

1. Crystal structure, reflective spectrum, Raman spectra and photoresponsivity of SiP flake

To gain a deep understanding of the electronic properties of the WSe_2/SiP hetero-interface, we provide detailed information on the two-dimensional van der Waals SiP material. As schematically shown in Fig. S1, the SiP crystal exhibits an anisotropic orthorhombic layered structure (space group of $Cmc2_1$) with a monolayer thickness of 6.7 Å, anti-parallel stacked with an interlayer spacing of 3.6 Å along the z direction. In each monolayer, there are three inequivalent structural units in which Si–Si dumbbells are surrounded by distorted antiprisms made of P atoms. These structural units are connected by sharing P atoms arranged along the y direction but replicated along the x direction. As a result, the lattice constants of the SiP crystal are very different along the x and y directions, leading to the remarkable anisotropic properties therein. The rectangular lattice of the SiP crystal exhibits lattice parameters along the x direction $a_{\mathrm{SiP},x}$ = 3.53 Å and along the y direction $a_{\mathrm{SiP},y}$ = 20.56 Å. Therefore, the reciprocal momenta take values of $\boldsymbol{G}_{\mathrm{SiP},1}$ = 17.8 × $(1, 0)$ nm^{-1} and $\boldsymbol{G}_{\mathrm{SiP},2}$ = 3.05 × $(0, 1)$ nm^{-1} for SiP.

Specifically, three important spatial symmetry operations should be addressed in this atomic structure of the SiP crystal. First, although the atomic structure of monolayer SiP is inversion symmetric, there is no inversion symmetry in the SiP crystal due to anti-parallel layer stacking, providing an opportunity to identify the crystal orientation of SiP flakes based on second harmonic generation measurements (more details are discussed later). Second, there is mirror symmetry perpendicular to the x direction in the SiP crystal. This vertical mirror should enforce the spin photocurrent only along the direction perpendicular to the mirror. Third, there is a nonsymmorphic two-fold (C_{2v}) rotational symmetry about the z direction (and combined with half-unit-cell translation along the z direction, $C_{2z} + z/2$) in the SiP

crystal. This nonsymmorphic rotation symmetry of bulk SiP should enforce the complete cancelation of the spin photocurrent in any direction under the same incident circular polarization. Therefore, in our experiment, the symmetry operation of the SiP flakes (20 to 40 nm in thickness, whose properties are close to those in their bulk form) will prohibit spin current generation (more details are discussed later). Considering the WSe_2/SiP interface, the symmetry of monolayer SiP is important, and its inversion symmetry also prohibits the generation of spin photocurrent in monolayer SiP.

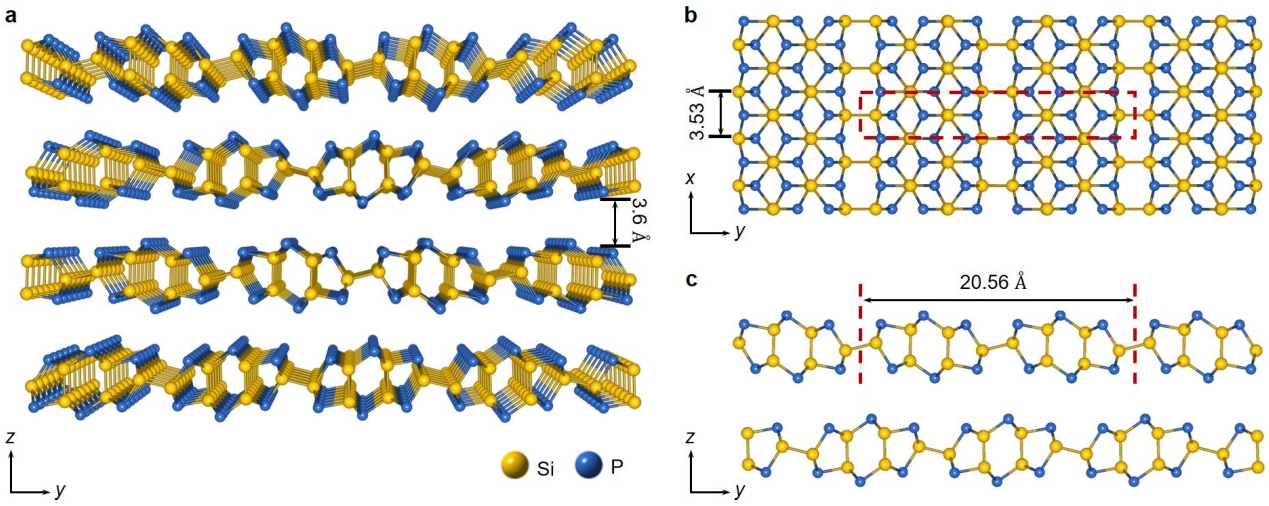

Fig. S1 | Crystal structure of SiP. a, Schematic figure of van der Waals SiP crystal. The yellow and blue balls represent Si and P atoms. The monolayers are anti-parallel stacked with an interlayer spacing of 3.6 Å. **b**,**c**, Top and side views of the SiP crystal. The in-plane unit cell is rectangular with $a_{\mathrm{SiP},x}$ = 3.53 Å and $a_{\mathrm{SiP},y}$ = 20.56 Å.

To investigate the anisotropic properties of the SiP crystal, we performed polarization-dependent reflection and Raman spectra measurements by using a confocal Raman microscopy system (WITec Alpha 300) with a 50× Olympus objective lens for a small spot size of incident light less than 2 μm^2. The spectra were collected by a spectrometer with a grating of 150 mm^{-1} for the reflection spectra (or

1800 mm^{-1} for the Raman spectra) under nonpolarized white light (or a linearly polarized laser of 532 nm whose polarization angle can be tuned by rotating a half-wave plate). An aperture was used during reflection spectra measurement to ensure that the reflected light was fully from the sample. A linear polarizer was used as an analyzer to select the polarization of the signal for the polarization-dependent measurements. All measurements were performed at room temperature in the atmosphere with an integration time of 20 seconds and accumulated 5 times.

The polarization-dependent reflection spectra can reveal the anisotropic properties of the optical absorption process in SiP crystals. At each polarization angle of the analyzer, the reflection spectra of the sample were obtained by normalizing the recorded data with the reflection spectra of the substrate, and the polarization-dependent reflection spectra are presented in Fig. S2a, in which all curves are normalized to the reflection spectrum at the 0°-rotated analyzer (polarization is parallel to the y direction of the SiP crystal). One can see a dip feature in the serial reflection spectra, centered near the band gap value of 1.819 eV of the SiP crystal, while a sharp peak feature near 2.12 eV is attributed to the influence of the silicon substrate. Specifically, the normalized reflection intensities at the energy of the SiP band gap display a π-period depending on the polarization angle (a two-fold rotational symmetry, as shown in the polar plot in Fig. S2b), directly indicating the anisotropic feature of the absorption at the band edge of the SiP crystal.

The polarization-dependent Raman spectra can show the anisotropic properties of the phonon vibration modes in the SiP crystal. A typical Raman spectrum was measured under nonpolarized conditions and is shown in Fig. S2c, in which the Raman shift values of the main Raman peaks are labeled accordingly. These Raman peaks show anisotropic features under polarized conditions. At each polarization angle

of the incident light, the polarization-dependent Raman spectra were obtained with the polarization of the analyzer parallel to the incident light. As a result, the intensities of these Raman peaks varying with the polarization angle are plotted in a colored map, as shown in Fig. S2d. One can see that there are two groups of Raman vibration modes, namely, the A_1 and A_2 modes, which are classified by two-fold and four-fold rotational symmetry depending on the polarization angle. Specifically, for the six main Raman peaks labeled in Fig. S2c, the polar plots of the A_1 modes (e.g., 261, 301, 553 cm^{-1}) clearly show two-fold rotational symmetry (Fig. S2e). In sharp contrast, the polar plots of the A_2 modes (114, 141, 464 cm^{-1}) clearly show four-fold rotational symmetry (Fig. S2e). These results clearly reveal the clear dependence of the Raman spectra on the crystalline orientation and the strong anisotropy of the phonon vibration modes in the SiP crystal.

The anisotropic atomic structure of the SiP crystal can further cause the anisotropic optoelectronic response therein. The anisotropic photocurrent generated from the SiP crystal along the *x* and *y* directions and the polarization-dependent photocurrent along each direction of the SiP crystal are shown in Fig. S3a and b. On the one hand, along each direction of the SiP crystal, there is a remarkable difference in the measured photocurrent values under bias voltage V_{ds} = 6 V between the two states of light "on" and "off" during the manual switching process. Note that based on the crystal symmetry of SiP, the non-symmorphic two-fold (C_{2v}) rotational symmetry about the *z* direction should enforce the complete cancellation of the photovoltaic or photogalvanic effect in either the *x* or *y* direction under incident light normal to the sample. As a result, the observed switching between the "on" and "off" states of the photocurrent in the SiP crystal directly indicates photo-induced electronic conductivity therein. Compared with the photocurrent values between the *x* and *y* directions under the same incident polarization of light, one can see that the photocurrent of the SiP crystal shows anisotropic features,

indicating anisotropic electronic transport properties. On the other hand, along each direction of the SiP crystal, the photocurrent values clearly depend on the polarization of the incident light. In both the *x* and *y* directions, the photocurrent values with a polarization angle of 0° are larger than those with a polarization angle of 90°. This polarization-dependent photocurrent in the SiP crystal can be attributed to the anisotropic optical absorption therein (Fig. S2a). Such anisotropic optoelectronic responses directly show the potential of SiP as a polarization-sensitive photodetector.

To demonstrate the capability of the SiP crystal as a photodetector, we determined the response photon energy and photoresponsivity of the SiP photodetector. One can see in Fig. S3c that the photocurrent displays an increasing tendency with decreasing photon energy. Importantly, a dip feature is clearly found at a photon energy near 1.8 eV (photon energy is close to the band gap of 1.819 eV for SiP crystal), indicating inter-band optical transition cutoff at the band edge. A resonant photocurrent peak appears near 1.63 eV (photon energy is below the band gap of 1.819 eV for SiP crystal), possibly originating from the excitonic states and the impurity level therein. Specifically, under incident light with a wavelength of 532 nm, the photocurrent response is linearly proportional to the light intensity and can be detected down to the pA level when the light intensity is as small as 10 nW (Fig. S3d). As a result, the photocurrent can be detected in a wide intensity range over three orders. Note that the photocurrent shows a strong polarization dependence, in which the anisotropic ratio can be enhanced, reaching 3.13 at a small intensity of 100 nW. Such intensity-dependent photocurrent and photon energy-dependent photoresponsivity demonstrate that SiP can function as a photodetector working over a wide wavelength range and intensity range. Nevertheless, the optoelectronic response and photocurrent values of SiP are much smaller than those of excellent monolayer transition metal

dichalcogenides, such as WSe_2. Therefore, at the WSe_2/SiP hetero-interface, the measured photocurrent is mainly contributed by the monolayer WSe_2.

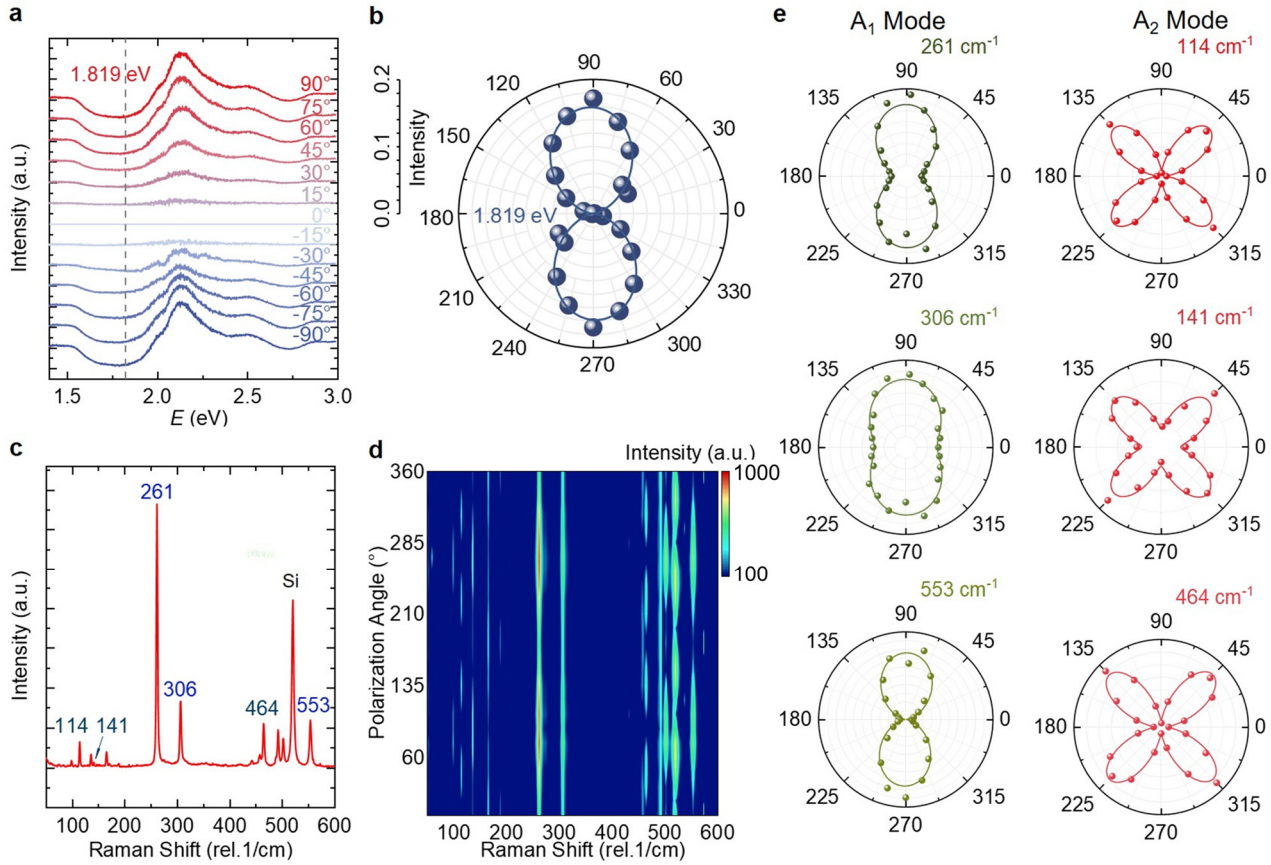

Fig. S2 | Polarization-dependent reflection and Raman spectra of SiP flake. **a**, Reflection spectra under nonpolarized white light with different polarization angles of the analyzer. These reflection spectra are normalized to the reflection spectrum polarization angle of 0° (parallel to the *y* direction of the SiP crystal). **b**, Polar plots of normalized reflection intensities of the SiP flake. The reflection spectra show a clear two-fold symmetry for the band edge absorption of the SiP crystal. **c**, Raman spectrum of SiP crystal. The Raman shift values of the main Raman peaks are provided, and the Raman peaks of the silicon substrate are labeled. There are two types of Raman vibrational modes denoted as A_1 and A_2 modes. **d**, Colored mapping of the Raman peak intensities as a function of the Raman shift values and the polarization angles. **e**, Polar plots of Raman intensities for SiP flakes. The A_1 and A_2 modes are classified by the two-fold and four-fold symmetries, respectively.

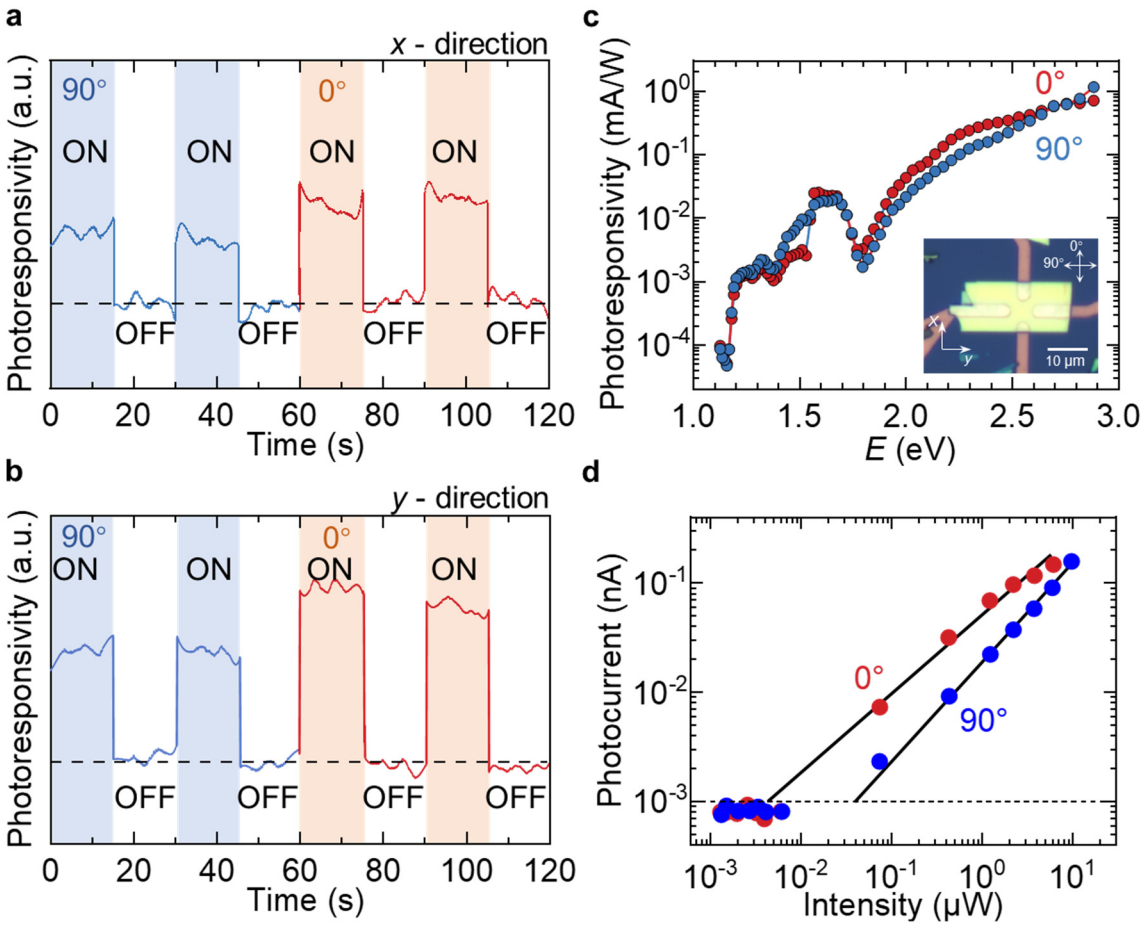

Fig. S3 | Photoresponse properties of the 2D SiP photodetector. a, Time-dependent photoresponse of the SiP photodetector with photocurrent along the *x* direction under linearly polarized light (532 nm) at polarization angles of 0° (polarization parallel to the *y* direction) and 90° (polarization perpendicular to the *y* direction). **b**, Time-dependent photoresponse of the SiP photodetector with photocurrent along the *y* direction under linearly polarized light (532 nm) at different polarization angles. In both directions, the photocurrent depends on the polarization angles. **c**, Photoresponsivity depending on the excitation energy of the SiP photodetector. The polarization angles of incident light are 0° and 90°, and the detected photocurrent is along the *y* directions of the SiP crystal. **d**, Laser intensity-dependent photocurrent of the SiP photodetector. The polarization angles of incident light are 0° and 90°, and the detected photocurrent is along the *y* directions of the SiP crystal.

2. Second harmonic generation and identification of twist angles at the WSe_2/SiP hetero-interface

The second harmonic generation measurement was performed using a Ti:sapphire oscillator, with the fundamental excitation set to 810 nm, pulse width of 70 fs, and repetition rate of 80 MHz. The laser pulse was focused to a spot size of ~1 μm on the sample by a 40× objective lens. The polarization direction of the incident beam was varied using a polarizer and a half-wave plate, which was initially aligned with the mirror plane (*y* direction) of monolayer WSe_2 and the SiP flake. The linear polarization of the second harmonic light was selected and analyzed by individual polarizers and half-wave plates in the detection path, and the generated second harmonic light was detected by a photomultiplier tube. The second harmonic signals were obtained under the condition that the polarizations of the input and output lights were parallel to each other.

To experimentally identify the twist angles and confirm the existence of mirror symmetry at the WSe_2/SiP hetero-interface, we performed second harmonic generation (SHG) measurements to identify the crystal orientation of each monolayer of WSe_2 and SiP flakes. Since the twisted angle between the monolayer WSe_2 and SiP flake determines the existence of the mirror symmetry at the WSe_2/SiP hetero-interface, the results of polarization-resoled second harmonic generation as a function of the polarization angle for the monolayer WSe_2, the SiP flake and the WSe_2/SiP hetero-interface are shown in Fig. S4. One can see in Fig. S4a that the schematic crystal structures of monolayer WSe_2 and SiP have distinct rotational symmetries of C_{3v} and C_{2v} rotational symmetry. Note that the point group of isolated monolayer WSe_2 is D_{3h}, and here, we only focus on the rotational symmetries around the *z*-axis and the vertical mirror symmetries therein to consider the interface

symmetry between WSe_2 and other two-dimensional materials, or the symmetry of gated WSe_2. These two different rotational symmetries are incompatible, and therefore, the WSe_2/SiP hetero-interface will have no rotational symmetry. Specifically, by tuning the twist angle, the mirror symmetry of the hetero-interface can be selectively maintained, as shown in Fig. S4b, in which the 0°-twisted WSe_2/SiP hetero-interface maintains mirror symmetry, while the 90°-twisted WSe_2/SiP hetero-interface does not.

Specifically, taking the 0°-twisted WSe_2/SiP hetero-interface as an example (Fig. S4c), the second harmonic generation signal of this hetero-interface displays a distorted six-fold rotational symmetry, whose orientation is identical to that of monolayer WSe_2. The SiP flake shows a two-fold rotational symmetry, whose orientation is found to align to that of monolayer WSe_2, and the orientation mismatch is found to be less than one degree. As a result, this hetero-interface can be determined to have C_{1v} symmetry. In sharp contrast, for the 90°-twisted WSe_2/SiP hetero-interface (Fig. S4d), the orientation of the two-fold rotational symmetry of the SiP flake is found to be orthogonal to that of the six-fold rotational symmetry of monolayer WSe_2, confirming the absence of mirror symmetry at this particular hetero-interface. In this way, the symmetry of different hetero-interfaces can be determined. When the twisted angle between the monolayer WSe_2 and the few-layer SiP is 0°, the symmetry of the hetero-interface can thus be distinguished with a single mirror.

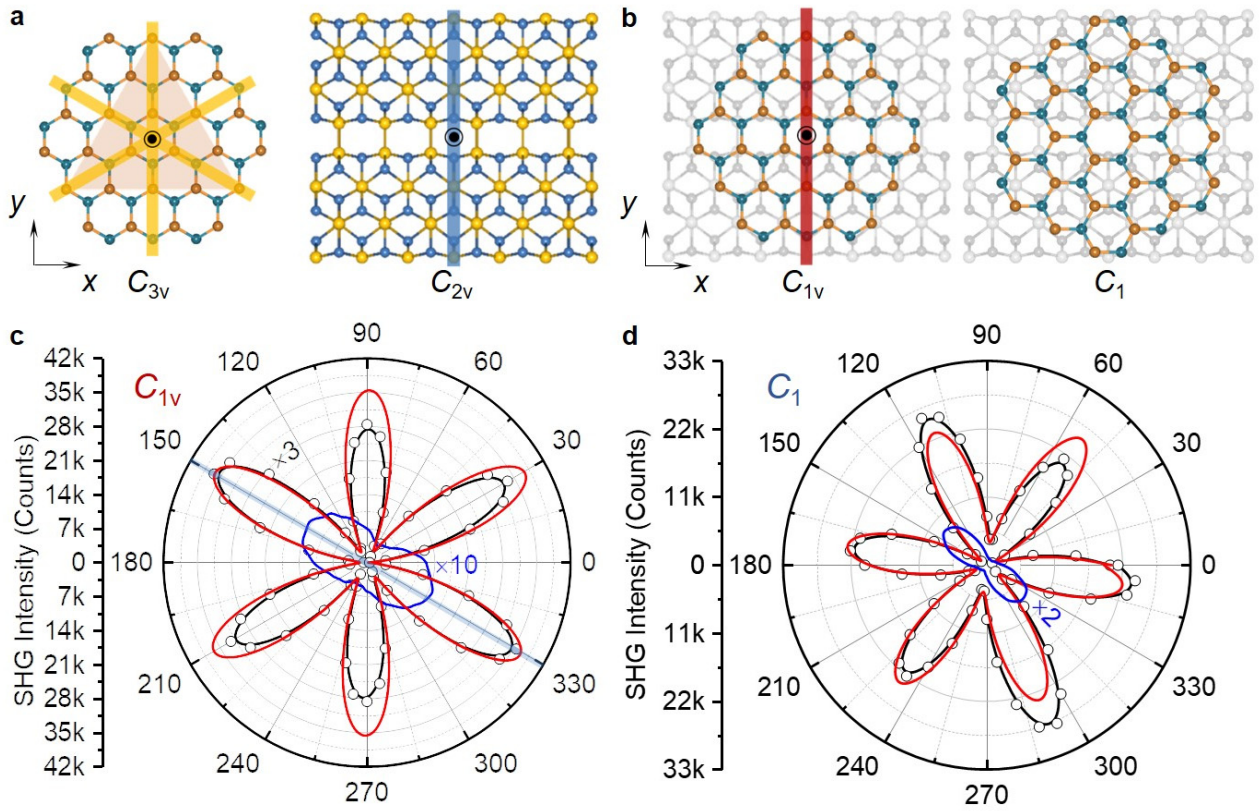

Fig. S4 | SHG results for the crystal orientation of WSe_2/SiP hetero-interfaces. a, Schematic crystal structure of monolayer WSe_2 with C_{3v} rotational symmetry (left) and SiP with C_{2v} rotational symmetry (right). Yellow and blue lines represent vertical mirror planes therein. Circled dots represent rotational axes. The light red triangle represents the C_{3v} rotational symmetry of monolayer WSe_2. **b**, Schematic figures of the crystal structure of the 0°-twisted WSe_2/SiP hetero-interface with C_{1v} symmetry (left) and the 90°-twisted WSe_2/SiP heterointerface with C_1 symmetry (right). The red line represents the mirror plane. **c**, Polar plots of the polarization-resolved second harmonic intensity (black circle) as a function of the polarization angle of WSe_2/SiP with C_{1v} symmetry. The red and blue lines are the second harmonic intensities of the individual monolayer WSe_2 and SiP flake, respectively. **d**, Polar plots of the polarization-resolved second harmonic intensity (black circle) as a function of the polarization angle of WSe_2/SiP with C_1 symmetry. The red and blue lines are the second harmonic intensities of the individual monolayer WSe_2 and SiP flake, respectively.

3. Example of data analysis process for spin photocurrent

To make the fitting details clear to the reader, we provided the fitting analysis process in Fig. S5 based on the equation $J = C\sin 2\varphi + L_1 \sin 4\varphi + L_1 \cos 4\varphi + D$, where C accounts for the spin photocurrent originating from the inter-band Berry curature dipole, L_1 and L_2 account for the linear photocurrent corresponding to the shift current and thermal photocurrent, and D accounts for a polarization-independent photocurrent. Taking the raw data of the polarization-independent photocurrent at the WSe_2/SiP hetero-interface (Fig. S5a, red points) as an example, the photocurrent values under left-handed circularly polarized light (φ = 45°) and right-handed circularly polarized light (φ = 135°) are found to be different, indicating an obvious spin photocurrent component ($C\sin 2\varphi$) therein. Such a spin photocurrent component can be quantitatively obtained from the raw data with Fourier analysis, as shown in Fig. S5b, in which the red circles in a sine curve represent the spin photocurrent component of the raw data. The amplitude of such a sine curve indicates the value of C in the fitting equation. Similarly, the linear photocurrent component ($L_1\sin 4\varphi + L_2\cos 4\varphi$) can be obtained with the same analysis (Fig. S5c, red circles). In sharp contrast, the spin photocurrent component obtained from the raw data of the bare WSe_2 (Fig. S5a, blue points) is shown by the blue circles in Fig. S5b, in which the amplitude of the spin photocurrent component is small, but the linear photocurrent component (blue circles in Fig. S5c) is obvious. With this analysis, one can conclude that the spin photocurrent generated from the WSe_2/SiP hetero-interface under normal incidence of light is reasonably large, in contrast to the zero spin photocurrent in bare WSe_2. The difference between the two cases is caused by the bottom SiP that breaks the rotational symmetry of monolayer WSe_2 in heterostructures. Therefore, this phenomenon indicates that interfacial symmetry plays an important role in spin photocurrent generation.

Similarly, the raw data of the photocurrent from the WSe_2/SiP hetero-interface measured at different gate voltages are shown in Fig. S5d (orange circles for $V_G > 0$ and red circles for $V_G < 0$). One can see that the photocurrent at $V_G < 0$ displays clearer oscillation than the photocurrent at $V_G > 0$, and spin photocurrent is significantly enhanced by applying a negative gate voltage. Based on the analysis, the photocurrent at $V_G < 0$ shows larger amplitudes of the spin photocurrent component (Fig. S5e) and linear photocurrent component (Fig. S5f) than those of the photocurrent at $V_G > 0$. As a result, the spin photocurrent generated from the WSe_2/SiP hetero-interface is confirmed to be gate-tunable.

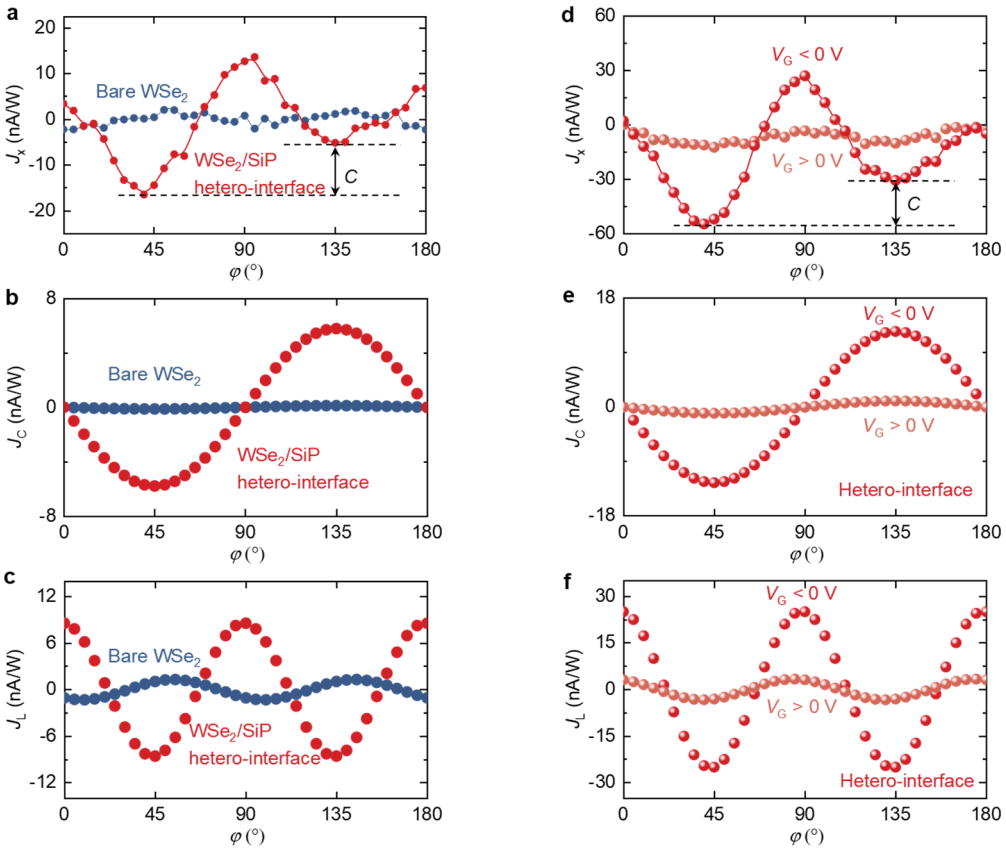

Fig. S5 | Example of data analysis process for spin photocurrent. a, The raw data of photocurrent measurements for bare WSe_2 and WSe_2/SiP hetero-interface. **b**,**c**, Fittted spin photocurrent component (b) and linear photocurrent component (c) obtained from raw data in (a). **d**, The raw data of gate-dependent photocurrent measurements for WSe_2/SiP hetero-interface. **e**,**f**, Fittted spin photocurrent component (e) and linear photoccurrent component (f) from data in (d).

4. Position-dependent spin photocurrent at the WSe_2/SiP hetero-interface

To measure the spin photocurrent, we established a photocurrent measurement system. The optical path of the measurement setup is schematically shown in Fig. S6, in which a supercontinuum source (SC-Pro-7) with an acousto-optic tunable filter (AOTF) option for single wavelength output (pulsed laser with tunable pulse repetition frequency from 10 kHz to 80 MHz, linewidth of 2–10 nm with linear polarization) from 430 nm to 1400 nm was used. The polarization state of the near-infrared laser can be tuned by rotating a quarter-wave plate to switch between left-handed (φ = 45°) and right-handed (φ = 135°) circular polarization. The photocurrent signal was measured under periodic switching of light illumination with a frequency of 233 Hz fed from the chopper. All photocurrent measurements were performed at room temperature in the atmosphere.

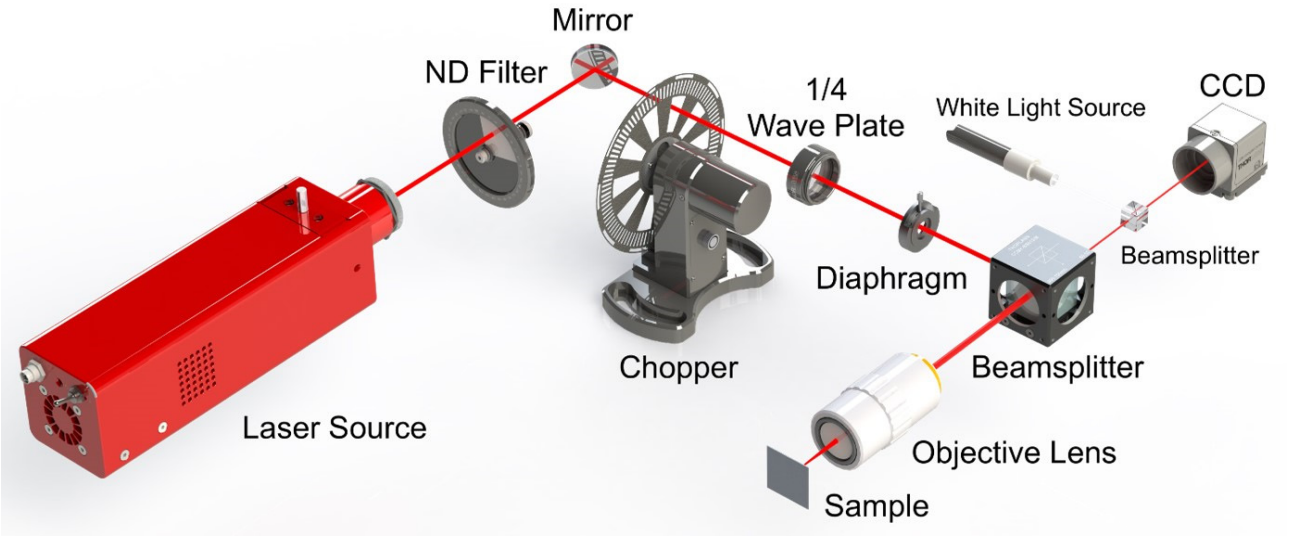

Fig. S6 | Schematic figure for the optical measurement setup of the spin photocurrent measurement system. A supercontinuum source was used to generate the spin photocurrent under periodic switching of light illumination via chopper. The drawing files for each optical element of optical photocurrent measurement setup are obtained from Thorlabs website.

To confirm that the spin photocurrent is generated from the WSe_2/SiP hetero-interface, we swept the laser spot across two electrodes in the zero-biased WSe_2/SiP hetero-interface device (Fig. S7a) with a fixed incident direction normal to the sample (z direction) by moving the sample position with a linear translation stage. The position-dependent spin photocurrent J_C is shown in Fig. S7b. Specifically, at each position of the laser spot, the photocurrent value depending on the rotating angle of the quarter-wave plate is shown in Fig. S7c. Compared with the small spin photocurrent generated on the Ti/Au electrodes on both sides, the spin photocurrent takes the maximum value when the laser is shinning on the center position between the two electrodes. Such a dome shape of the position-dependent spin photocurrent clearly confirms that the spin photocurrent is generated from the hetero-interface.

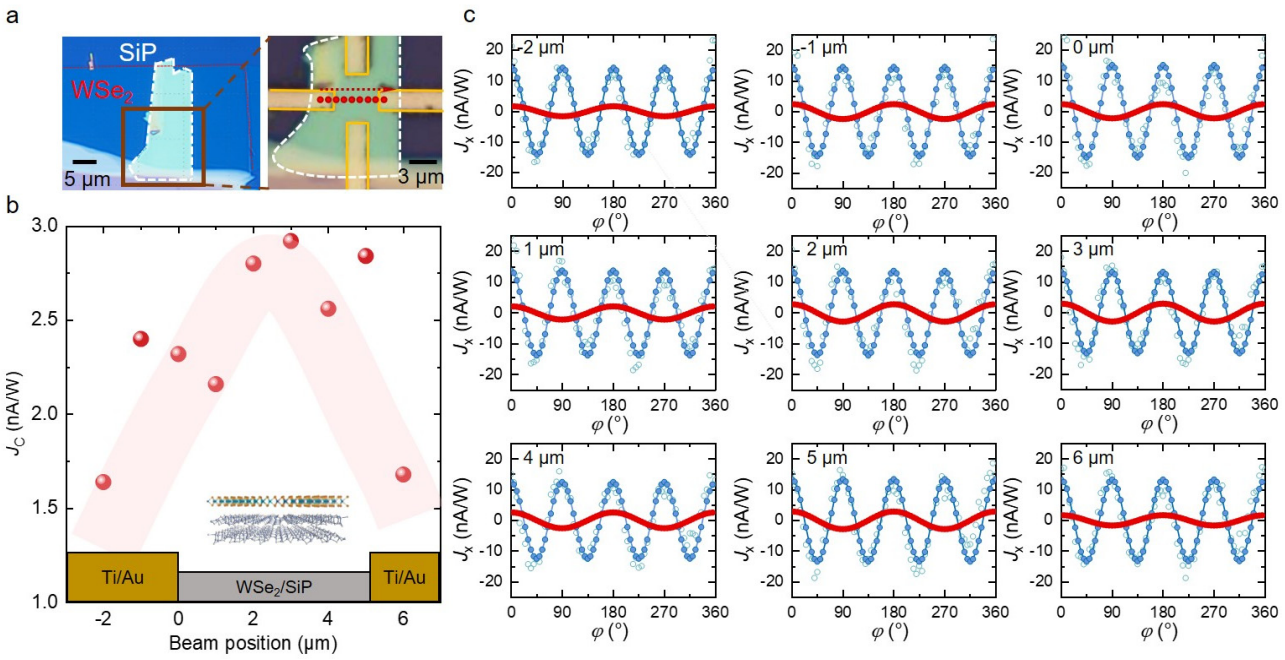

Fig. S7 | Position-dependent photocurrent at the WSe_2/SiP hetero-interface. **a**, Optical microscopic images of the hetero-interface (left) and the device (right). The monolayer WSe_2 is transferred on top of the SiP flake, and the region of the hetero-interface is highlighted by the white dashed lines. The red dashed arrow represents the sweeping direction of the laser spot. **b**, Position-dependent spin photocurrent. The dome shape of the position-dependent spin photocurrent clearly confirms that the spin photocurrent is generated from the hetero-interface. **c**, The photocurrent value depending on the rotating angle of the quarter-wave plate at each position of the laser spot (for λ = 1064 nm, V_{ds} = 0 V, V_G = 0 V, and the laser incidence direction is fixed in the *z* direction).

5. Absence of spin photocurrent in pristine monolayer WSe_2 and SiP flake

To confirm the generation of the spin photocurrent at the WSe_2/SiP hetero-interface, we measured the spin photocurrent of the monolayer WSe_2 and SiP flakes for comparison. Measurements were done with the same situation (V_{ds} = 0 V, V_G = 0 V) under incident light (λ = 1064 nm) normal to the sample in the z direction. For the spin photocurrent of monolayer WSe_2 (Fig. S8a), the photoresponsivity varies with the rotating angle φ of the quarter-wave plate with a basically $\frac{\pi}{2}$-period (Fig. S8b). As a result, the values of the photoresponsivity at right and left-handed circularly-polarized lights are found to be similar, directly indicating that the spin photocurrent component C (with π-period) is negligibly small, while the linear photocurrent components (L_1 and L_2) dominate. We claim that there is no obvious spin photocurrent component C from the bare WSe_2, since the value of C = 0.1 ± 0.7 nA/W, whose value of 0.1 is smaller than the magnitude of the error bar of 0.7 (the error bars are defined by the residual values of Fourier analysis for original data). With this analysis from the data statistics, the signal will be regarded to be zero from the viewpoint of statistics in photocurrent measurements. This is simply because the C_{3v} symmetry of monolayer WSe_2 will enforce the complete cancellation of the spin photocurrent in any direction under the same incident circular polarization.

Similarly, for the spin photocurrent of the SiP flake (Fig. S8c), there is no π-period in the photoresponsivity as a function of the rotating angle φ of the quarter-wave plate (Fig. S8d), and the values of the photoresponsivity at right-handed and left-handed circularly-polarized lights are almost identical. There is the same symmetry confinement for the SiP flake: the nonsymmorphic C_{2v} symmetry of the SiP crystal completely prohibits the generation of spin photocurrent therein. Therefore, spin photocurrent cannot be generated in SiP and monolayer WSe_2.

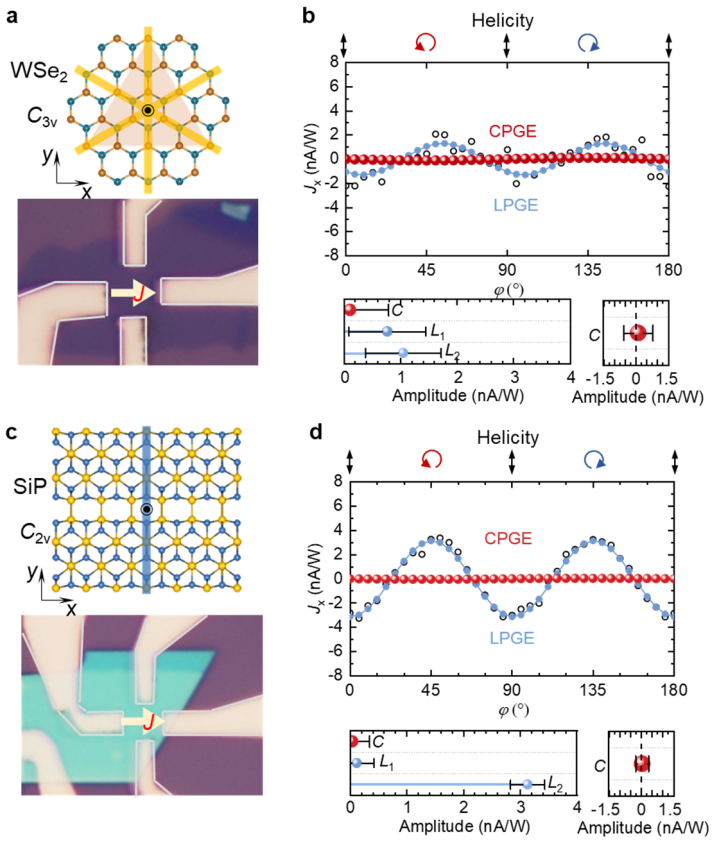

Fig. S8 | Spin photocurrent in monolayer WSe_2 and SiP with the laser incident in the *z* direction. **a**, Schematic crystal structure of C_{3v} symmetric monolayer WSe_2 (upper part) and optical microscopic image of the device (lower part). The white arrow indicates the direction of the measured spin photocurrent. **b**, The photoresponsivity of monolayer WSe_2 as a function of the rotation angle φ of the quarter-wave plate (for λ = 1064 nm, V_{ds} = 0 V, V_G = 0 V). Black open circles denote the obtained data. Red and blue balls denote the spin photocurrent component and the linear photocurrent component, whose amplitudes C, L_1 and L_2 are shown in histograms in the lower panel. **c**, Schematic crystal structure of C_{2v} symmetric monolayer SiP (upper panel) and optical microscopic image of the device (lower panel). **d**, The photoresponsivity of the SiP flake as a function of the rotation angle φ of the quarter-wave plate (for λ = 1064 nm, V_{ds} = 0 V, and V_G = 0 V). Data are presented as mean values +/− error bar, in which the error bar is defined by the residual values of error analysis in Fourier series expansion for the original data of 37 data points in the range from 0° to 180°.

6. Laser intensity-dependent spin photocurrent at the hetero-interface

To confirm that the spin photocurrent is linearly dependent on the laser intensity, we performed spin photocurrent measurements with different incident laser intensities (shown in Fig. S9). The amplitudes of the spin photocurrent component C increase linearly with the incident light intensity I over a wide range from 3 to 3000 μW, confirming that they originate from a second-order optoelectronic response to the electric field $\boldsymbol{E}$ of light ($|\boldsymbol{E}|^2 \propto I$); thus, the spin photocurrent component C is proportional to $|\boldsymbol{E}|^2$ (the exponent values are found to be close to 1). This result is consistent with the spin photocurrent contributed by the topologically nontrivial origin of the BCD at this hetero-interface with such low symmetry.

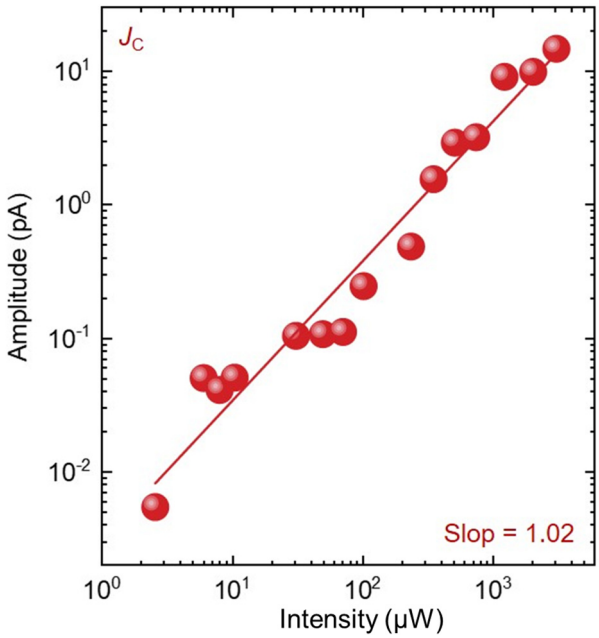

Fig. S9 | Laser intensity-dependent spin photocurrent at the WSe_2/SiP hetero-interface. Laser intensity-dependent amplitudes of the spin photocurrent component C (red balls). The exponent value is approximately 1 by the fitted line.

7. Spin photocurrent based on oblique incidence angles

To elucidate the details of the helicity-to-spin conversion process at the heterointerface with C_{1v} symmetry, we measured the spin photocurrent for the C_1 symmetric WSe_2/SiP hetero-interface under different incident light directions (shown in Fig. S10, oblique angles θ are measured from the *z* direction). The generated spin photocurrents J_x (along the *x* direction) and J_y (along the *y* direction) at the C_1 symmetric WSe_2/SiP hetero-interface can be qualitatively expressed by the unit vector $\boldsymbol{e}$ pointing in the propagation direction of light, as discussed in Table 1 in the main text.

In the case of the incident light in the *xz* plane (Fig. S10a) with oblique angle θ, the spin photocurrent J_x can be described phenomenologically as $J_x = \beta_{11}e_x + \beta_{13}e_z$, while the spin photocurrent J_y can be described as $J_y = \beta_{21}e_x + \beta_{23}e_z$, in which e_x and e_z represent the components of the propagation direction of the incident light in Cartesian coordinates. As a result, both the values of the spin photocurrent J_x and J_y are strongly dependent on the oblique angle θ of the incident light, as shown in Fig. S10b. Correspondingly, in the case of incident light in the *yz* plane (Fig. S10c), the spin photocurrent J_x can be described phenomenologically as $J_x = \beta_{12}e_y + \beta_{13}e_z$, while the spin photocurrent J_y can be described as $J_y = \beta_{22}e_y + \beta_{23}e_z$. Therefore, both values of the spin photocurrent J_x and J_y vary with the oblique angle θ (Fig. S10d). As a result, the generation of spin photocurrent is consistent with the symmetry analysis (Table 1 in the main text). The spin photocurrent at oblique angle of 30° is shown in Fig. 2 in the main text because a higher oblique angle causes practical difficulty in identifying the position of laser spot.

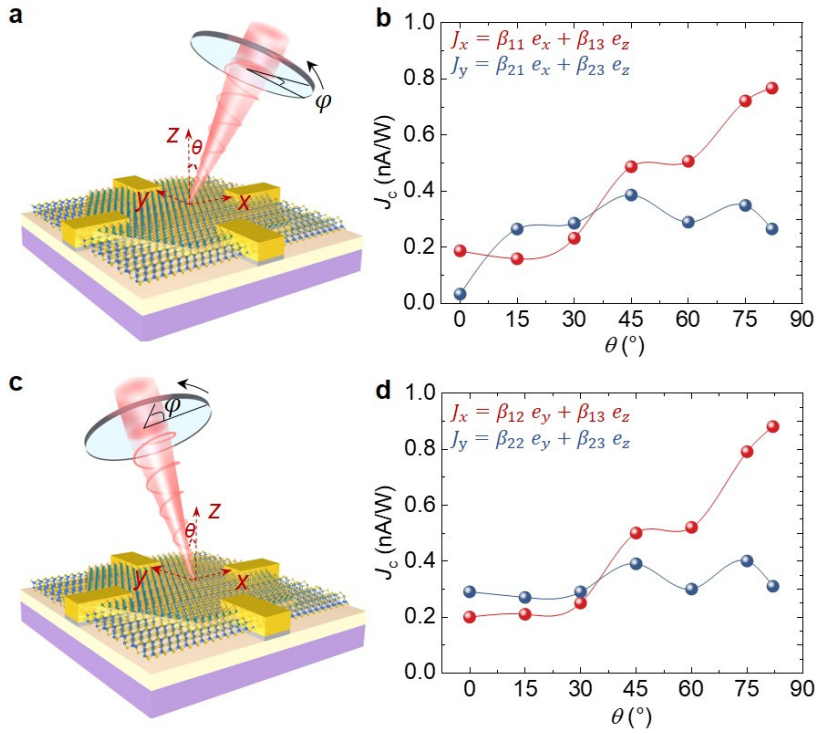

Fig. S10 | Spin photocurrent based on oblique incidence angles. a, Schematic configuration of incident light in the *xz* plane. The generated spin photocurrent J_C is measured along the *x* direction for J_x and along the *y* direction for J_y. **b**, The spin photocurrent J_x (red) and J_y (blue) as functions of the oblique angle θ of the incident light (λ = 1064 nm, V_{ds} = 0 V, V_G = 0 V). **c**, Schematic configuration of incident light in the *yz* plane. **d**, The spin photocurrent J_x (red) and J_y (blue) as functions of the oblique angle θ of the incident light (λ = 1064 nm, V_{ds} = 0 V, V_G = 0 V). Note that the amplitude of the spin photocurrent may vary with the position of the laser spot while changing the oblique angle.

8. The amplitude of the photocurrent as a function of excitation energy and back gate voltage

To clearly show the mechanism of the drop in the amplitude of the spin photocurrent with increasing gate voltage, we thus provide additional data of the polarization-independent photocurrent D as a function of photon energy and gate voltage. In principle, in the observed photocurrent $J = C\sin 2\varphi + L_1 \sin 4\varphi + L_1 \cos 4\varphi + D$, the photocurrent J can be decomposed by the spin photocurrent component C (with a period of π with respect to the rotating angle of the quarter-wave plate φ), the linear photocurrent components L_1 and L_2 (with a period of $\pi/2$) and the polarization-independent photocurrent component D, according to different microscopic mechanisms and optical selection rules in the optical absorption processes. All of those components (depending on the polarization of light) are strongly dependent on the density of the initial and final states in the optical transition processes. Therefore, the amplitudes of C, L_1, L_2 and D will show similar tendencies (actually a universal behavior) when blocking the final states with Fermi level tuning in the band structure.

One can see that both the amplitudes of spin photocurrent (Fig. S11a) and polarization-independent photocurrent (Fig. S11b) show similar behavior with the applied gate voltage (Fig. S11c). Such similarity of these gate-tuning behaviors indicates that the decrease in the optical absorption when blocking the final states in the optical transition is actually a universal mechanism not only for the spin photocurrent and linear photocurrent but also for the polarization-independent photocurrent. Note that the Fig. 4b in the main text is plotted for the spin photocurrent amplitude as a function of excitation energy and back gate voltage, in which the interpolation of third-order polynomial is used for the anti-aliasing of the image. We thus provide the figure with a zero-order polynomial (without any interpolation) in Fig. S12.

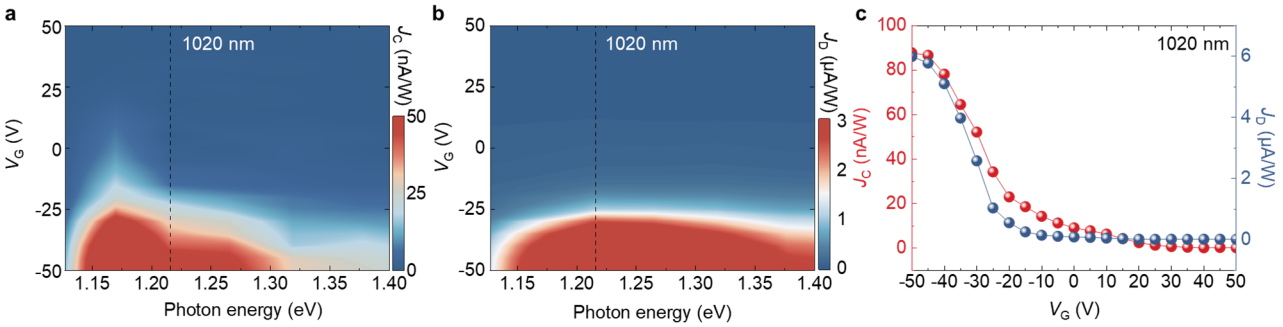

Fig. S11 | Amplitude of spin photocurrent and polarization-independent photocurrent as a function of photon energy and gate voltage. a–c, Both the amplitude of the spin photocurrent (a) and the polarization-independent photocurrent (b) near 1.22 eV (light wavelength of 1020 nm) can be significantly enhanced by applying the negative gate bias (c). Such a similarity of the gate-tuning behavior indicates that the decreased optical absorption with blocking the final states in the optical transition is actually a universal mechanism not only for the spin photocurrent and linear photocurrent but also for the polarization-independent photocurrent.

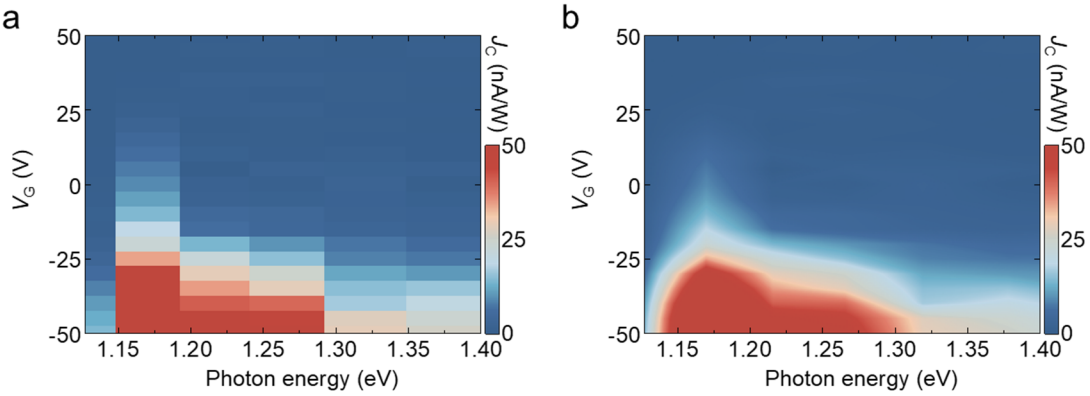

Fig. S12 | Colored mapping of the spin photocurrent component as a function of excitation energy and back gate voltage with normal-incident light (V_{ds} = 0 V). a,b, The mappings are interpolated by a zero-order polynomial (a) and a third-order polynomial (b).

9. Gate-dependent photoluminescence of monolayer WSe_2 and gate transfer curve of hetero-interface device

To show that the Fermi level can be tuned by gate voltage, we performed measurements of the gate-dependent photoluminescence of the WSe_2 A-exciton and trion at 78 K and the gate transfer curve of the WSe_2/SiP hetero-interface device at room temperature, as shown in Fig. S13. One can see that the intensity of the WSe_2 A-exciton and trion can be tuned by applying a back gate voltage, indicating the electron/hole doping of monolayer WSe_2 in which the Fermi level of monolayer WSe_2 can be effectively tuned by the back gate. According to our independent transport measurement, one can clearly see that the WSe_2/SiP hetero-interface device is in the "on state" with the Fermi level within the valence band and is in the "off state" with the Fermi level within the band gap. The critical gate voltage values to turn on the electronic state in the transfer curves match well with those in the gate-dependent spin photocurrent curves.

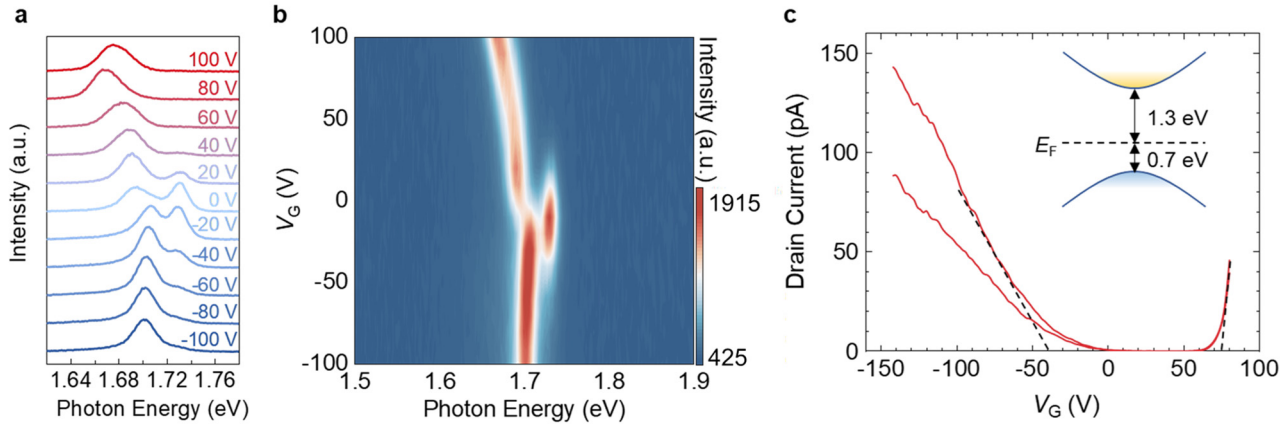

Fig. S13 | The gate-dependent photoluminescence of the WSe_2 and the gate transfer curve of the WSe_2/SiP hetero-interface device. a,**b**, The gate-dependent photoluminescence of monolayer WSe_2 (a) and the colored mapping of the intensity as a function of back gate voltage and the emission energy (b) at 78 K. **c**, The gate transfer curve of the WSe_2/SiP hetero-interface device at room temperature.

10. Formation of Moiré subbands at the hetero-interface

In the main text, the indirect **intra-band** transition describes the optical transition from the initial states to the final states, both of which are within the valence band **in the Brillouin zone of monolayer WSe_2 without considering WSe_2 Brillouin zone folding**. While the direct **inter-band** transition describes the optical transition from the initial states in the Moiré subband to the final states in the valence band maximum **in the Moiré Brillouin zone of the WSe_2/SiP hetero-interface with considering WSe_2 Brillouin zone folding**. When Brillouin zone folding is taken into account, the indirect **intra-band** transition at different momenta becomes the direct **inter-band** transition at the same momenta.

In the first model description, the optical transition at 1.2 eV is designated as the **intra-band** transition in the Brillouin zone of the WSe_2 monolayer because our experiments have confirmed that both the initial and final states of the optical transition are located within the valence band with the following two pieces of evidence. 1) We intentionally chose the excitation energy of light below the energy of the band gap of monolayer WSe_2, and thus, there is no optical transition from the WSe_2 valence band to its conduction band. In this case, there is only an intra-band optical transition within the valence band since WSe_2 is a *p*-type semiconductor at zero gate bias or we intentionally tune the sample into the *p*-type region by electrical gating. 2) Once the Fermi level (originally located in the valence band) is tuned up to a level inside the band gap, all the electronic states in the valence band are occupied, and there is no empty state serving as the final state in the optical transition. Thus, the obtained spin photocurrent can be "switched off", as shown in Fig. 4b in the main text. Therefore, both the initial and final states of the optical transition at 1.2 eV are confirmed to be located within the valence band, and the corresponding optical transition is regarded as the **intra-band** transition.

Note that due to the energy and momentum conservation laws, there is no direct optical transition at the same momenta near the K (−K) points in the Brillouin zone of monolayer WSe_2, the above-mentioned intra-band optical transition should be an indirect transition in the valence band of WSe_2, and the initial state to final state in the valence band will be located at different momenta. To satisfy the momentum conservation law of optical transition, the role of SiP (which creates the periodic Moiré potential at the WSe_2/SiP hetero-interface) must be properly considered. One can see that in Fig. S14a, the formation of the Moiré pattern induces new periodicity that generates replica bands with a distance of $\Delta \boldsymbol{k}_{\min}$ in momentum space at the K (−K) points in the Brillouin zone of monolayer WSe_2. Therefore, in the first model description **without considering WSe_2 Brillouin zone folding**, the **intra-band** optical transition is allowed by considering the reciprocal lattice vector (the crystal momentum) caused by the formation of the Moiré pattern.

In the second equivalent model description, with WSe_2 Brillouin zone folding, we properly consider the hybridization of the electronic states associated with the reciprocal lattice vector, which is caused by the SiP-induced Moiré potential. As shown in Fig. S14b, those electronic states are hybridized and form Moiré subbands. Therefore, in the folded Brillouin zone with formed Moiré subbands, the optical transition at 1.2 eV is described as the direct **inter-subband** transition from the occupied electronic state in the Moiré subbands near the valence band bottom to the empty electronic state in the Moiré subbands at top of the valence band. This picture describing the optical transition with the Moiré subbands in the folded Brillouin zone is schematically shown in the inset of Fig. 4a in the main text.

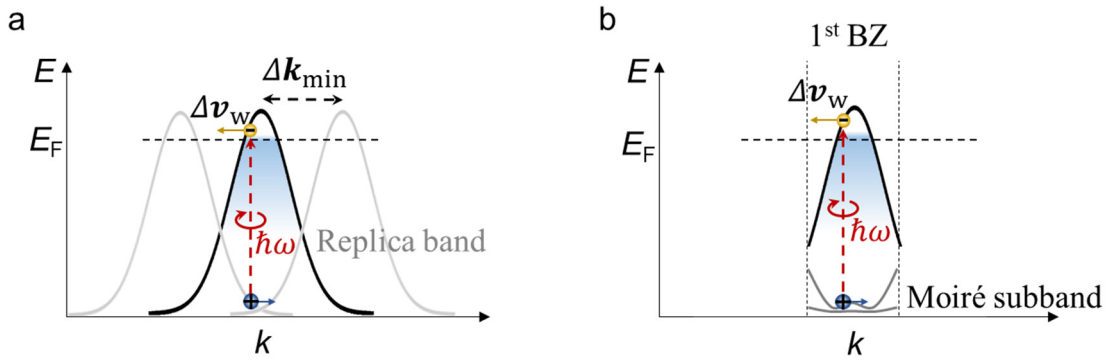

Fig. S14 | Two equivalent models for describing the same optical transition with and without Brillouin zone folding. a, The transition within the valence band viewed in the original WSe_2 band basis in the Brillouin zone (BZ) of WSe_2 caused by the periodic Moiré potential, which couples different replica bands without considering Brillouin zone folding. **b**, The same transition viewed in the Moiré subband basis (by diagonalizing the band Hamiltonian with the periodic Moiré potential) with considering Brillouin zone folding.

11. Temperature-dependent measurement of the spin photocurrent at the hetero-interface

As discussed above, the intra-band optical transition is not truly phonon-assisted but is assisted by reciprocal lattice vector induced translation symmetry breaking to the leading order. Theoretically, we believe that the phonon-assisted spin photocurrent generation is a higher-order effect that will be greatly suppressed. This is because such a process involves an intermediate state where an electron absorbs/emits a phonon (before or after absorbing a photon), which changes the momentum but almost not the energy of an electron. Since the initial (final) electron state must be filled (empty) for such a process, such electron states are constrained to the vicinity of the Fermi surface, and the phonon momentum has to match the Fermi momentum shift. This highly constrains the phase space of such processes and thus suppresses their contribution to the spin photocurrent generation.

To understand the role of phonon in the spin photocurrent generation, we performed gate-dependent spin photocurrent measurements on the WSe_2/SiP hetero-interface at low temperature and provided the results in Fig. S15a. Even at a low temperature of 10 K, at which the phonon might not play a key role in the intra-band optical transition, the amplitude of the spin photocurrent still displays clear V_G-dependent behavior, and the spin photocurrent can be "switched on" by tuning the Fermi level down in the band structure with a negative V_G. If we compare the V_G-dependent behavior of spin photocurrent amplitude at 10 K to that at room temperature (Fig. 4c in the main text), one can see a similar tendency in their curves of the V_G-dependent amplitude of spin photocurrent (the spin photocurrent amplitude increases with decreasing V_G). Such a similarity (the spin photocurrent amplitude depending on the Fermi level position in the band structure) indicates that the spin

photocurrent in the WSe_2/SiP hetero-interface is intrinsic and can be well explained even without considering the role of phonons.

To provide additional evidence that the phonon does not play a significant role in the spin photocurrent generation, we performed temperature-dependent spin photocurrent measurements at $V_G = -45$ V and 0 V (Fig. S15b,c), at which the optical transitions are remarkably different, with the Fermi levels below and above the valence band maximum. One can see that at $V_G = -45$ V with the Fermi level below the valence band maximum, the amplitude of the spin photocurrent remains finite at low temperature. In sharp contrast, at $V_G = 0$ V with the Fermi level located above the valence band maximum, the spin photocurrent amplitude decreases rapidly to almost zero with cooling temperature. This is because of the following scenario: the electronic states below the Fermi level have a larger occupation probability with cooling (the Fermi–Dirac distribution is a function of temperature), and thus, the density of empty electronic states at the valence band maximum decreases with decreasing temperature. As a result, for both spin photocurrent measurements at $V_G = -45$ V and 0 V, the spin photocurrent amplitude shows similar decreasing behavior with temperature cooling. Therefore, the temperature-dependent spin photocurrent amplitude strongly relies on the Fermi level position in the band structure, and the phonon mechanism might not play a significant role in the spin photocurrent generation.

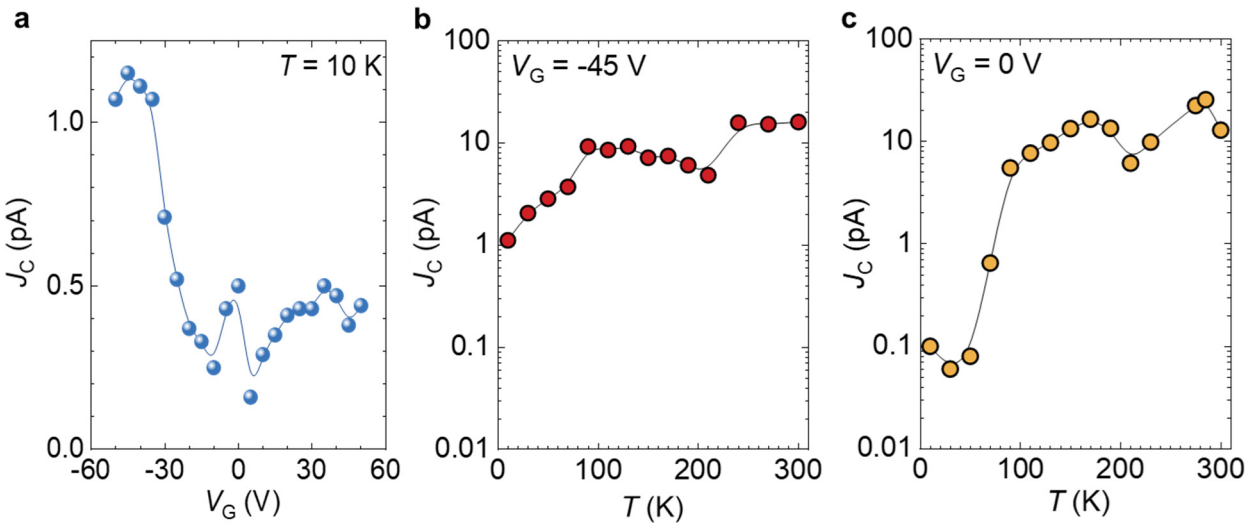

Fig. S15 | Temperature-dependent spin photocurrent amplitude of the hetero-interface. a, Gate-dependent amplitude of spin photocurrent at 10 K with normal incidence of light, in which the amplitude of spin photocurrent is enhanced when applying a negative gate voltage. **b**, Temperature-dependent amplitude of spin photocurrent at $V_G = -45$ V. The spin photocurrent amplitude decreases with cooling and remains finite at low temperature. **c**, Temperature-dependent amplitude of spin photocurrent at $V_G = 0$ V. The spin photocurrent amplitude decreases with cooling and vanishes rapidly at low temperature. The temperature-dependent spin photocurrent amplitude strongly relies on the Fermi level position in the band structure, and the phonon mechanism might not play a significant role in the spin photocurrent generation.

12. Reproducibility of the spin photocurrent generation at the hetero-interface

To show that our results based on WSe_2/SiP hetero-interface under normal-incident light are highly reproducible, all the experiments were performed in multiple samples (Fig. S16). The spin photocurrent generation has been widely achieved if there is no metal/semiconductor contact issue for electronic measurement in fabricated devices. To prove the reproducibility of the directional selectivity of the generated spin photocurrent at the C_{1v} symmetric hetero-interface, we show spin photocurrent measurement results in two different samples in Fig. S17. Under normal incidence of light, the generated spin photocurrent is along the *x* direction (perpendicular to the mirror of the hetero-interface), while it vanishes along the *y* direction (parallel to the mirror). These distinctive results from different samples indicate the same phenomenon that mirror symmetry is crucial in determining the direction of the generated BCD and the resulting spin photocurrent at symmetry-mismatched hetero-interfaces. Their similar behavior of directional selectivity of spin photocurrent proves the reproducibility of the interfacial symmetry dependence of spin photocurrent at the heterointerface.

To prove the reproducibility of the gate-dependent amplitude of spin photocurrent at the hetero-interface, we show the spin photocurrent measurement with the gate voltage tuned in three different samples (Fig. S18). One can see that the spin photocurrent in different samples displays similar "switched on" behavior when V_G is applied negatively. Such precise tuning of the Fermi level position in the band structure of the hetero-interface and the gate-dependent amplitude of spin photocurrent can be observed and show similar behavior in different samples, confirming the reproducibility of the gate tunability of the spin photocurrent.

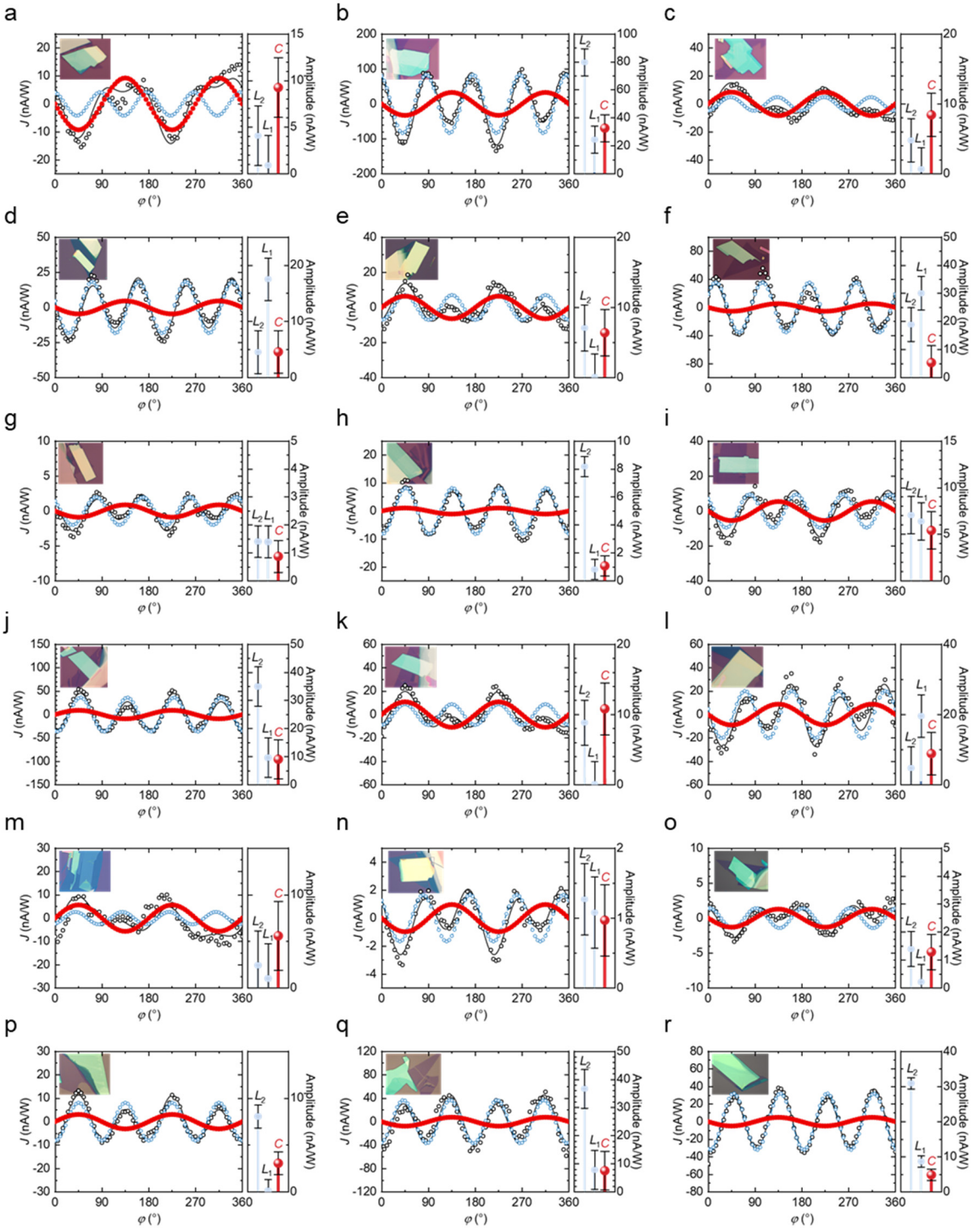

Fig. S16 | Reproducibility of spin photocurrent generation at WSe_2/SiP hetero-interfaces under normal incidence of light. a–**r**, The spin photocurrent was measured at different WSe_2/SiP hetero-interfaces with C_1 symmetry. Inset: optical microscopic images of the WSe_2/SiP hetero-interfaces. Data are presented as mean values +/− error bar (error bar is defined by the residual values of error analysis in Fourier series expansion for the original data of 73 data points in the range from 0° to 360°).

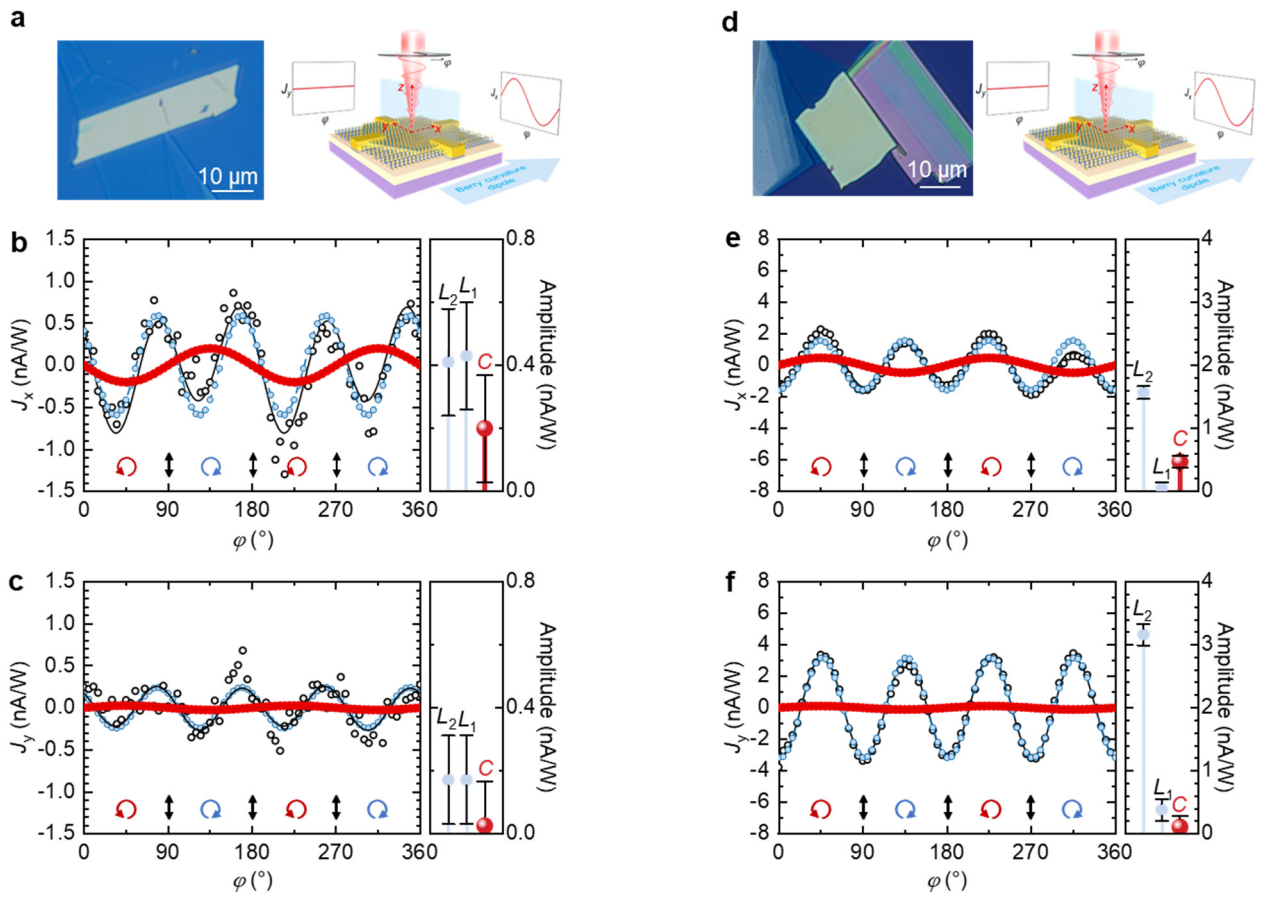

Fig. S17 | Reproducibility of the directional selectivity of the generated spin photocurrent for two different samples with C_{1v} symmetry. a, Optical microscopic image of the WSe_2/SiP sample and the measurement geometry under normal incidence of light. **b**,**c**, The generated spin photocurrent is along the *x* direction (perpendicular to the mirror), while it vanishes along the *y* direction (parallel to the mirror). Data are presented as mean values +/− error bar, and the error bar is defined by the residual values of error analysis in Fourier series expansion for the original data of 73 data points in the range from 0° to 360°. **d**, Optical microscopic image of another sample and the measurement geometry under normal incidence of light. **e**,**f**, The generated spin photocurrent is along the *x* direction (perpendicular to the mirror), while it vanishes along the *y* direction (parallel to the mirror). Data are presented as mean values +/− error bar, and the error bar is defined by the residual values of error analysis in Fourier series expansion for the original data of 73 data points in the range from 0° to 360°.

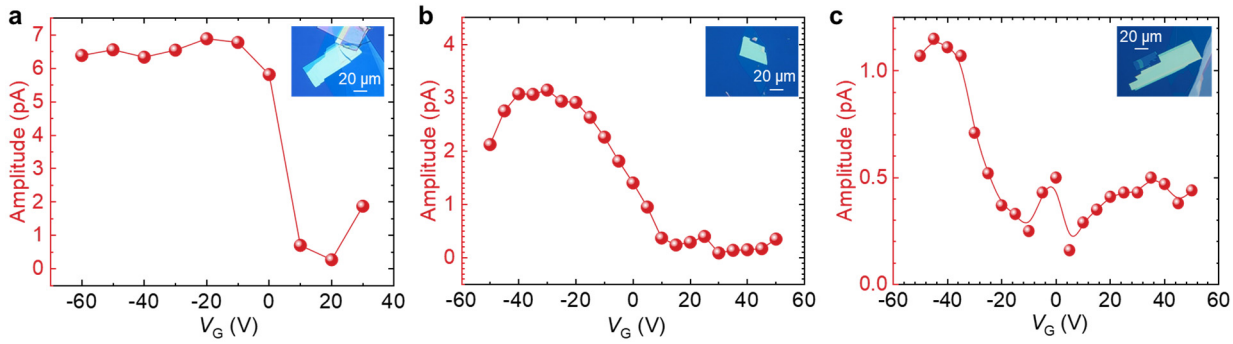

Fig. S18 | Reproducibility of the gate-tunablity of spin photocurrent for three different samples. **a–c**, The gate-dependent spin photocurrent at WSe_2/SiP hetero-interface at room temperature (a and b) and at 10 K (c). Inset: optical microscopic images of three different WSe_2/SiP samples.

13. Robustness of spin photocurrent against the extrinsic in-plane electric field

To show that the spin photocurrent intrinsically originates from the Berry curvature dipole of the hetero-interface device, we intentionally induce the extrinsic asymmetry by tuning the source-drain bias V_{ds}. A colored mapping of the spin photocurrent component C varying with the in-plane electric field and the back gate voltage V_{G} is shown in Fig. S19 (incident light normal to the sample of λ = 1064 nm with V_{G} in the range from −50 to 50 V. The in-plane electric field ranging from −0.6 to 0.6 V/μm is applied by the source-drain bias V_{ds} in range from −3 to 3 V). One can see two distinctive regions for the value of the spin photocurrent: the zero value region (marked in blue) and the large value region (marked in red).

The spin photocurrent values are mainly dependent on the back gate voltage V_{G} and thus the position of the Fermi level, while they are comparatively independent of the source-drain bias V_{ds} and thus the external electric field. Specifically, when V_{ds} is set at −2.7, 0 and 2.7 V, the gate-dependent spin photocurrent exhibits almost identical behavior (more details are shown in Fig. S20), indicating the robustness of the intrinsic spin photocurrent at this hetero-interface. Specifically, with increased V_{G}, the amplitude of the spin photocurrent increases from approximately 2 pA at V_{G} = −50 V to a maximum value of approximately 3 pA V_{G} = −30 V and then rapidly decreases to almost zero (V_{G} > 10 V). Such a spin photocurrent modulation indicates a clear electrical tuning of the magnitude of the BCD at the hetero-interface since the amplitude of spin photocurrent should be proportional to the magnitude of the BCD, as mentioned above. Since the excitation energy in our measurement is smaller than the band gap of monolayer WSe_2, all the optical transition paths are limited within the valence band, and the final states should be above the Fermi level due to Pauli blockade. This gate-tunable spin

photocurrent can be understood as follows if we consider the optical transition process. When the Fermi level is located above the valence band maximum (V_G > 10 V), there are no available final states for intra-band transition, and the BCD is zero. Therefore, the spin photocurrent can be electrically "switched off". On the other hand, as the Fermi level is set below the valence band maximum (V_G < 10 V), spin photocurrent is generated due to the large magnitude of the BCD.

Importantly, variation range (±3 V) of V_{ds} values is much larger than the height of Schottky barrier (normally less than the band gap value), yet the spin photocurrent does not differ from the situation of zero V_{ds}, providing solid evidence to exclude extrinsic origins. Therefore, our observed spin photocurrent should originate from the Berry curvature dipole, which is an intrinsic property of the electronic band structure and is produced by interfacial symmetry engineering at this symmetry-mismatched hetero-interface.

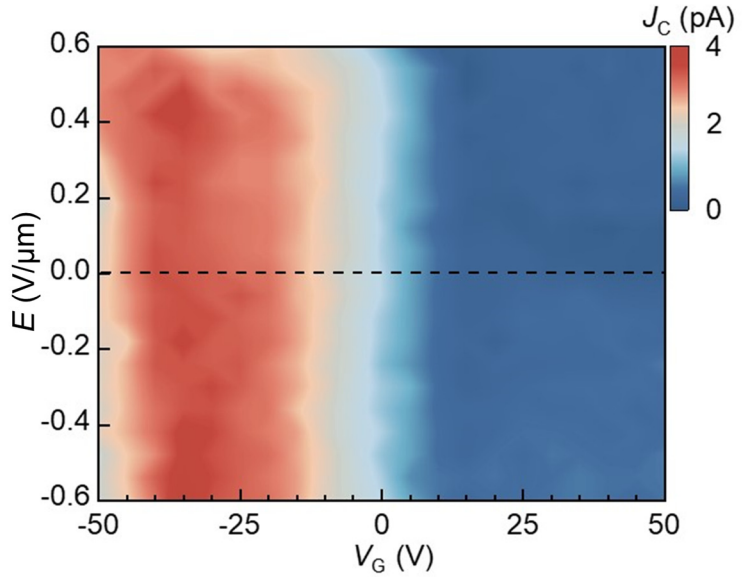

Fig. S19 | Colored mapping of spin current at various V_{ds} and V_G conditions. The spin photocurrent J_C is measured under incident light in the *z* direction.

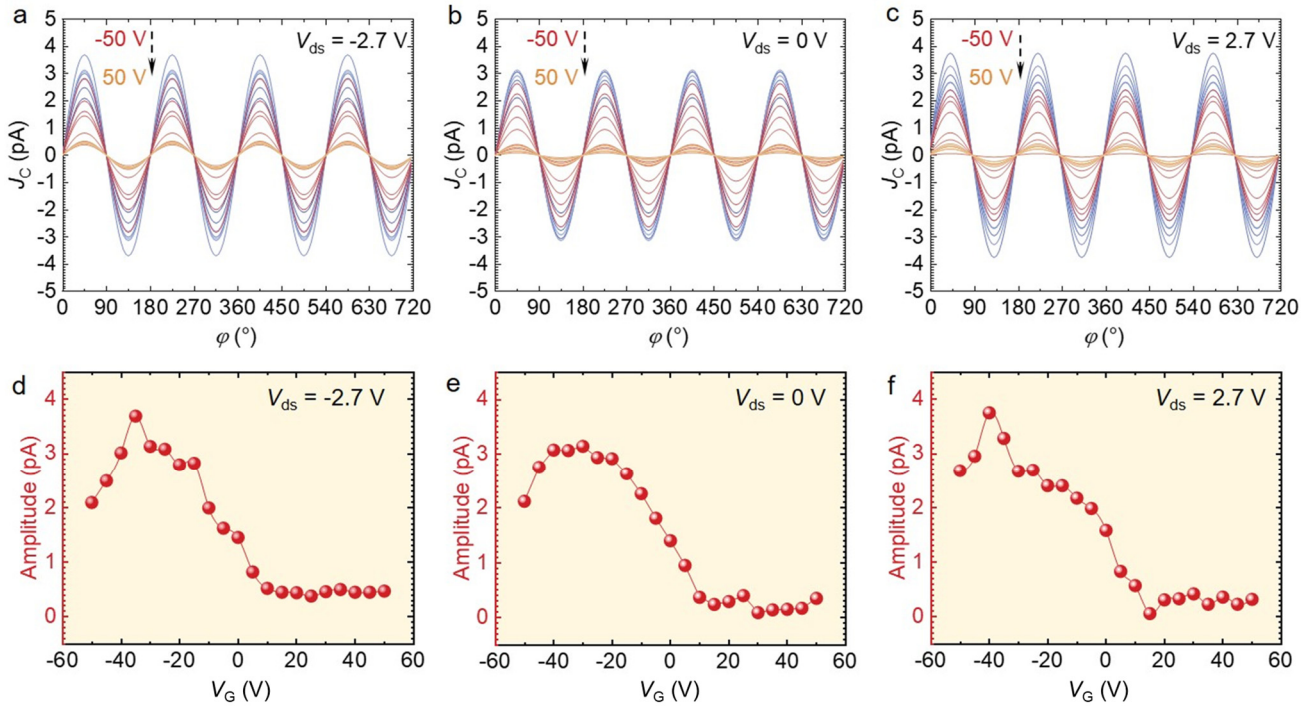

Fig. S20 | Spin photocurrent at the hetero-interface with different V_{ds} and V_G. a–c, The spin photocurrent J_C as a function of V_G ranging from −50 to 50 V of V_{ds} = −2.7 V (a), 0 V (b) and 2.7 V (c), respectively. **d–f**, V_G modulation of spin photocurrent component at V_{ds} = −2.7 V (d), 0 V (e) and 2.7 V (f). The spin photocurrent is generated with incident light normal to the WSe_2/SiP hetero-interface.

14. Spin photocurrent measurement with magnetic electrode

To experimentally confirm that such a photocurrent at the WSe_2/SiP hetero-interfaces is spin polarized, we designed a new control experiment to measure the generated spin photocurrent with magnetic electrodes based on the spin filter effect. We use Fe_3GeTe_2 thin flakes with an out-of-plane magnetic easy axis as the magnetic electrodes and further apply a perpendicular magnetic field to control the magnetization of these magnetic electrodes (Fig. S21a,b). Due to the spin filter effect, the magnetic electrode can be used to probe the high or low current states once the magnetization is parallel or antiparallel to the spin polarization of the injected current.

Note that we obtained two pieces of experimental evidence to confirm that the observed spin photocurrent is spin-polarized. 1) One can see in Fig. S21c,d that once the magnetization of the Fe_3GeTe_2 electrode is flipped by switching the direction of the magnetic field at ±550 mT (at 100 K below the Curie temperature of Fe_3GeTe_2), the amplitude of the generated spin photocurrent shows remarkably different values (high-current state J_C = 2.18 pA at −550 mT or low-current state J_C = 1.55 pA at 550 mT) corresponding to the different Fe_3GeTe_2 magnetizations parallel or antiparallel to the spin-polarization of the generated spin photocurrent. 2) The curve of the spin photocurrent amplitude as a function of the magnetic field shows an asymmetric shape (Fig. S21e). Due to the spin filter effect of the magnetic electrode whose magnetization magnitude is an odd function of the applied magnetic field, only in the case that the injected current is spin polarized, the magnetic electrode can probe the high or low current states with an asymmetric function of the magnetic field (Fig. S21f), which is consistent with what we observed experimentally. Therefore, these two observations provide experimental evidence that the generated spin photocurrent is spin polarized.

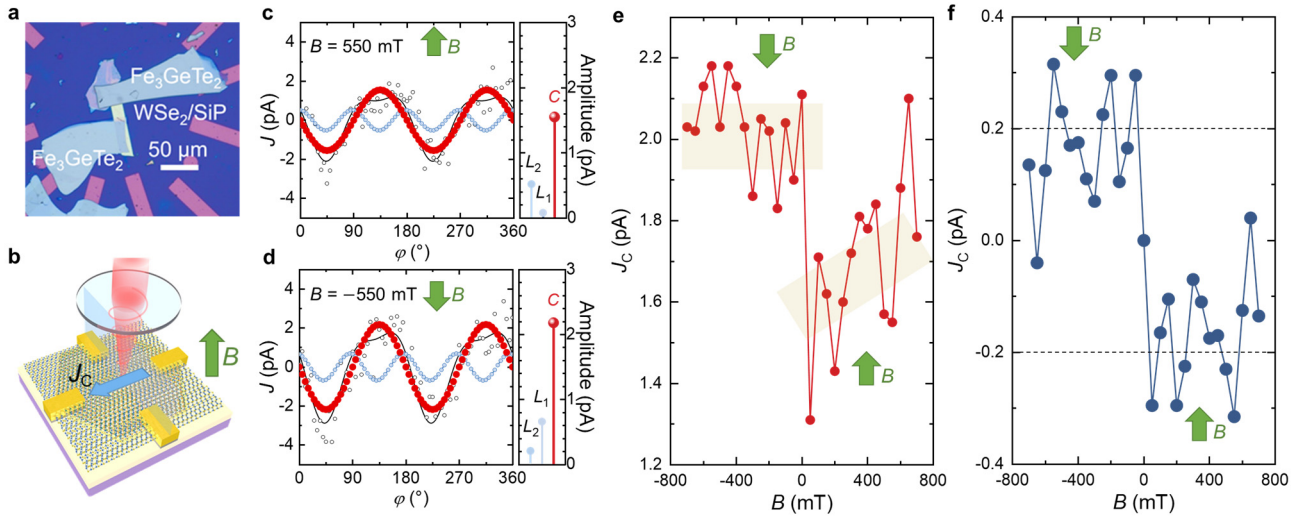

Fig. S21 | The amplitude of spin photocurrent as a function of magnetic field in the hetero-interface under normal incidence of light. a, Optical microscopic image of the WSe_2/SiP hetero-interface device with Fe_3GeTe_2 magnetic electrodes. **b**, Schematic measurement geometry, in which the magnetization of the Fe_3GeTe_2 electrode can be switched by applying a perpendicular magnetic field. **c**,**d**, The CPGE photocurrent measured at +550 mT with a CPGE amplitude of 1.55 pA, and it measured at −550 mT with a CPGE amplitude of 2.18 pA. The original data in each panel are shown with black open circles, and the total fitting function in each panel is shown with black lines. The spin photocurrent and linear photocurrent are shown with red and blue circles, respectively. Correspondingly, the fitted parameters of the spin photocurrent component C and linear photocurrent components (L_1 and L_2) are shown in the bar plot on the right side. **e**, The amplitude of spin photocurrent as a function of the applied magnetic field. **f**, The amplitude of spin photocurrent after the antisymmetrization process with $[J_C(+B) - J_C(-B)]/2$, which confirms that the spin photocurrent is spin polarized. The dashed lines highlight the tendency of the data, which shows a clear jump near zero magnetic field.

15. Phenomenological description of spin photocurrent and its relation with Berry curvature dipole at the hetero-interface

Phenomenological description of circular photogalvanic effect. The direct electrical current $\boldsymbol{J}$ induced by incident light, namely, the photocurrent, is a nonlinear response of the electronic system to the alternating external electric field $\boldsymbol{E}(\boldsymbol{r},t)$ of the incident light. Such photocurrent can be detected as photovoltaic or photogalvanic effects in an optoelectronic measurement. Here, we consider a monochromatic light incident on a sample with wave vector $\boldsymbol{q}$ and frequency ω. The alternating external electric field $\boldsymbol{E}(\boldsymbol{r},t)$ of the incident light can be expressed as $\boldsymbol{E}(\boldsymbol{r},t) = \boldsymbol{E}\exp(i\omega t - i\boldsymbol{q}\cdot\boldsymbol{r}) + c.c.$, in which i is the complex unit and $c.c.$ stands for the complex conjugate. With the help of Cartesian coordinates, the direct electrical current $\boldsymbol{J}$ in the photogalvanic effect can be generally expressed as a function of the electric field in second order:

$$J_a = \sigma_{abc}E_bE_c^*$$

where those subindices denote the components of the Cartesian coordinate, the superscript $*$ denotes the complex conjugate, and the σ_{abc} denotes the second order nonlinear conductivity for the photogalvanic tensor. Note that the Einstein summation convention is applied here, and the summation is understood over all three components of Cartesian coordinates for those subindices appearing twice within a single term.

Specifically, in the photogalvanic effect, the direct electrical current J_a is real and invariant under complex conjugate transformation. Therefore, $\sigma_{abc} = \sigma_{acb}^*$. Note that there is the permutation of the last two subindices of σ_{abc}, and thus the real part of σ_{abc} is symmetric under the operation of

exchanging b and c, while the imaginary part is antisymmetric with the same operation. To separate the above two contributions, the direct electrical current $\boldsymbol{J}$ in the photogalvanic effect can be rewritten as follows:

$$J_a = \sigma_{abc} E_b E_c^* = \frac{1}{2}\chi_{abc}(E_b E_c^* + E_c E_b^*) + i\beta_{ab}\epsilon_{bcd} E_c E_d^*$$

in which $\chi_{abc} = \chi_{acb}$, taking the role of the symmetric feature of σ_{abc}, the ϵ_{bcd} is the Levi–Civita tensor taking the role of the anti-symmetric feature of σ_{abc}, and thus the β_{ab} generally has no permutation features.

This expression shows that the direct electrical current $\boldsymbol{J}$ contains two different origins, depending on the electric field $\boldsymbol{E}$ of the incident light. The first term is symmetric and helicity-independent and thus can be classified as the linear photogalvanic effect. The second term is anti-symmetric and helicity dependent; thus, it switches its sign between left-handed and right-handed circularly-polarized incident light. As a result, the second term represents the circular photogalvanic effect, and β_{ab} is the coefficient tensor for the circular photogalvanic effect. To discuss the circular photogalvanic effect more clearly, the second term can be rewritten as follows:

$$(\boldsymbol{J}_{\mathrm{C}})_a = i\beta_{ab}(\boldsymbol{E} \times \boldsymbol{E}^*)_b = i\beta_{ab} e_b |\boldsymbol{E}|^2 P_{\mathrm{C}}$$

in which the unit vector $\boldsymbol{e}$ represents the propagation direction of the light and $P_{\mathrm{C}} = |\boldsymbol{E} \times \boldsymbol{E}^*|/|\boldsymbol{E}|^2 = \sin 2\varphi$ is the helicity of the light for the degree of circular polarization, varying between −1 (left-handed circularly-polarized light σ^-) and 1 (right-handed circularly-polarized light σ^+). This helicity of the light is a function of the delayed phase angle φ between the two components of the electric

field $\boldsymbol{E}$ of the light in the two orthogonal directions (i.e., E_x and E_y components when $\boldsymbol{e}$ points in the z direction) and thus can be tuned by rotating the quarter-wave plate in experiments.

Symmetry of spin photocurrent. Based on the spatial symmetry of crystals and without knowledge of the microscopic details, the direction and magnitude of the direct electrical current of the circular photogalvanic effect from a certain crystal can be determined by the angle of the incident light. Mathematically, each element of the circular photogalvanic tensor β_{ab} can be qualitatively known to be zero or nonzero, in which β_{ab} should be invariant under the symmetry operation of the crystal.

For the rotation symmetry along the z-axis R_z, the rotation operation for the θ angle takes the form:

$$R_z(\theta) = \begin{pmatrix} \cos\theta & \sin\theta & \\ -\sin\theta & \cos\theta & \\ & & 1 \end{pmatrix}$$

β_{ab} should be invariant under the rotation operation

$$\beta = R_z^{-1}(\theta)\beta R_z(\theta)$$

The C_{3v} symmetry contains an operation of the $2\pi/3$ rotation $R(2\pi/3)$, and therefore, the nonzero elements of β_{ab} take the form:

$$\beta = \begin{pmatrix} & \beta_{12} & \\ -\beta_{12} & & \\ & & \end{pmatrix}$$

in which there is only one independent variable.

The C_{2v} symmetry contains an operation of the π rotation $R(\pi)$, and therefore, the nonzero elements of β_{ab} take the form:

$$\beta = \begin{pmatrix} & \beta_{12} & \\ \beta_{21} & & \end{pmatrix}$$

in which there are only two independent variables.

The C_{1v} symmetry contains an operation of the reflection M (perpendicular to the x-axis); therefore, the nonzero elements of β_{ab} take the form:

$$\beta = \begin{pmatrix} & \beta_{12} & \beta_{13} \\ \beta_{21} & & \\ \beta_{31} & & \end{pmatrix}$$

in which there are only four independent variables.

For the C_1 symmetry, there is no symmetry operation, and therefore, the nonzero elements of β_{ab} take the form:

$$\beta = \begin{pmatrix} \beta_{11} & \beta_{12} & \beta_{13} \\ \beta_{21} & \beta_{22} & \beta_{23} \\ \beta_{31} & \beta_{32} & \beta_{33} \end{pmatrix}$$

in which there are nine independent variables.

Such phenomenological descriptions cannot reveal detailed information on the magnitude of elements of the circular photogalvanic tensor β_{ab} and their dependence on other tuning parameters, such as temperature and gate voltage. The magnitude of β_{ab} is the main target of the theory of the microscopic mechanism for the circular photogalvanic effect.

Microscopic origin of spin photocurrent and the Berry curvature dipole. In general, the generation of the circular photogalvanic effect involves two microscopic processes. First, when light is shed on the material, the photo-induced carriers are excited by left or right-handed circularly-polarized light

from the initial state to the final state governed by the optical selection rule. Second, those photo-excited carriers (including electrons and holes) will move with their group velocities accompanied by band dispersions, and thus, a net charge current appears by integrating all the photo-excited carriers in the Brillouin zone.

Our consideration here is general for both inter-band and intra-band optical transitions. We emphasize that the inter-band and intra-band here are defined with the monolayer WSe_2 conduction and valence bands (not the Moiré bands introduced below).

With the assumption of ignoring the momentum of the incident light (photon drag effect), the intra-band optical transition will be absent if there is no Moiré lattice potential from SiP (which breaks the momentum conservation in WSe_2, see definition of Moiré potential in Methods $\boldsymbol{k}\cdot\boldsymbol{p}$ model). In the presence of the SiP Moiré potential, the conduction and valence bands of WSe_2 will be folded and broken into smaller Moiré bands in a Moiré Brillouin zone (MBZ). For principle derivations, it is more convenient to work in the Moiré band basis, in which the quasi-momentum $\boldsymbol{k}$ in the MBZ is conserved in an optical transition (while the momentum in WSe_2 is not conserved). We use $n>0$ and $n<0$ to denote the $|n|$-th conduction and valence Moiré band (counted from the WSe_2 band gap), respectively. The spin photocurrent $\boldsymbol{J}_{\mathrm{C}}$ for the circular photogalvanic effect can then be expressed based on Fermi's golden rule:

$$\boldsymbol{J}_{\mathrm{C}}=-\frac{2\pi e\tau}{\hbar}\sum_{n_I<n_F}\int\frac{\mathrm{d}^2\boldsymbol{k}}{(2\pi)^2}\Delta\boldsymbol{v}(\boldsymbol{k})V(\boldsymbol{k})\delta[\Delta\varepsilon(\boldsymbol{k})-\hbar\omega]\Delta f(\mu,\boldsymbol{k})$$

In this equation, $\boldsymbol{k}$ is the MBZ quasi-momentum, $\boldsymbol{J}_{\mathrm{C}}$ is the difference between the photocurrents due to right-handed and left-handed circularly-polarized light (denoted as RCP and LCP light), τ is the

relaxation time, $V(\boldsymbol{k}) = |P_{\mathrm{RCP}}(\boldsymbol{k})|^2 - |P_{\mathrm{LCP}}(\boldsymbol{k})|^2$ describes the difference between the optical transition probability for RCP and LCP light, n_{I} and n_{F} are the Moiré band index of all possible initial states $|n_{\mathrm{I}}, \boldsymbol{k}\rangle$ and final states $|n_{\mathrm{F}}, \boldsymbol{k}\rangle$ (the MBZ quasi-momentum $\boldsymbol{k}$ will be abbreviated in most places hereafter for simplicity) that satisfy the energy conservation enforced by the δ function, and $\Delta\boldsymbol{v}(\boldsymbol{k})$, $\Delta\varepsilon(\boldsymbol{k})$ and $\Delta f(\mu, \boldsymbol{k})$ are the difference in the group velocity, energy, and Fermi-Dirac distribution between the initial and final states. Note that $n_{\mathrm{I}} < n_{\mathrm{F}}$, since the final state has higher energy than the initial state due to the absorption of photons. P, the optical transition dipole, is defined as

$$P = \frac{e}{m}\langle n_{\mathrm{F}}|\boldsymbol{A}\cdot\boldsymbol{p}|n_{\mathrm{I}}\rangle$$

where e and m are the charge and mass of a bare electron, $|n_{\mathrm{I}}\rangle$ and $|n_{\mathrm{F}}\rangle$ are the initial and final states, $\boldsymbol{A}$ is the vector potential of light and $\boldsymbol{p}$ is the momentum operator. The momentum operator $\boldsymbol{p}$ is defined as $p_a = \frac{\partial H}{\partial k_a}$, and thus, the full expression of $V(\boldsymbol{k})$ takes the form:

$$V(\boldsymbol{k}) = |P_{\mathrm{RCP}}(\boldsymbol{k})|^2 - |P_{\mathrm{LCP}}(\boldsymbol{k})|^2 = \left(\frac{e|\boldsymbol{A}|}{m}\right)^2 \left[\left|\langle n_{\mathrm{F}}|p_x + ip_y|n_{\mathrm{I}}\rangle\right|^2 - \left|\langle n_{\mathrm{F}}|p_x - ip_y|n_{\mathrm{I}}\rangle\right|^2\right]$$

$$= 2i\left(\frac{e|\boldsymbol{A}|}{m}\right)^2 \left[\langle n_{\mathrm{F}}|p_y|n_{\mathrm{I}}\rangle\langle n_{\mathrm{I}}|p_x|n_{\mathrm{F}}\rangle - \langle n_{\mathrm{F}}|p_x|n_{\mathrm{I}}\rangle\langle n_{\mathrm{I}}|p_y|n_{\mathrm{F}}\rangle\right]$$

where $|n_{\mathrm{I}}\rangle$ and $|n_{\mathrm{F}}\rangle$ are the Bloch wavefunctions of the possible initial and final states in the n_{I}-th and n_{F}-th Moiré bands (inter-Moiré band transition), and p_x and p_y are the momentum operators.

Recall that the Berry curvature for an N-band system (in 2D, the Berry curvature is only defined along the out-of-plane direction) is defined as

$$\Omega_z^n(\boldsymbol{k}) = i\sum_{n\neq n'} \frac{\left\langle n'\left|\frac{\partial H}{\partial k_x}\right|n\right\rangle\left\langle n\left|\frac{\partial H}{\partial k_y}\right|n'\right\rangle - \left\langle n'\left|\frac{\partial H}{\partial k_y}\right|n\right\rangle\left\langle n\left|\frac{\partial H}{\partial k_x}\right|n'\right\rangle}{[\varepsilon_n(\boldsymbol{k}) - \varepsilon_{n'}(\boldsymbol{k})]^2}$$

which is the sum of **all inter-band Berry curvatures of** $\boldsymbol{\Omega_z^n(k) = \sum_{n\neq n'} \Omega_z^{n,n'}(k)}$ where the inter-band Berry curvature $\Omega_z^{n,n'}(\boldsymbol{k})$ directly describes the virtual excitations between two bands. This directly indicates that $V(\boldsymbol{k})$ can be directly expressed by the inter-band Berry curvature of the initial and final states in two bands:

$$V(\boldsymbol{k}) = \frac{2e^2}{\hbar^2} A^2 \Omega_z^{\mathrm{F,I}}(\boldsymbol{k})[\Delta\varepsilon(\boldsymbol{k})]^2$$

The number of photoexcited carriers in *k*-space is thus directly proportional to the value of the inter-band Berry curvature of the initial or the final state. Therefore, the total direct electrical current can be obtained by integrating all the photoexcited carriers

$$J_{\mathrm{CPGE}} = -\frac{2\pi e\tau}{\hbar}\sum_{I,F}\int \frac{d^2k}{(2\pi)^2}\Delta\boldsymbol{v}(\boldsymbol{k})V(k)\delta[\Delta\varepsilon(\boldsymbol{k}) - \hbar\omega]\Delta f(\mu,\boldsymbol{k})$$

$$= -\frac{4\pi e^3\tau}{\hbar^3} I\int \frac{d^2\boldsymbol{k}}{(2\pi)^2}\frac{d\big(\Delta\varepsilon(\boldsymbol{k})\big)}{\hbar d\boldsymbol{k}}\Omega_z^{\mathrm{I,F}}(\boldsymbol{k})[\Delta\varepsilon(\boldsymbol{k})]^2\delta[\Delta\varepsilon(\boldsymbol{k}) - \hbar\omega]$$

$$\propto -\frac{e^3\tau}{\pi\hbar^2} I\int \frac{d^2\boldsymbol{k}}{(2\pi)^2}\frac{d\Omega_z^{\mathrm{I,F}}(\boldsymbol{k})}{\hbar d\boldsymbol{k}}\delta[\Delta\varepsilon(\boldsymbol{k}) - \hbar\omega]$$

One can see that only an imbalanced distribution of the inter-band Berry curvature at the Fermi level, which is nothing but the inter-band BCD, can result in a nonzero value of the direct electrical current J, where the magnitude of the inter-band BCD can be written as:

$$P_{\mathrm{BCD}} = \int \frac{\mathrm{d}^2\boldsymbol{k}}{(2\pi)^2}\frac{\mathrm{d}\Omega_z^{\mathrm{I,F}}(\boldsymbol{k})}{\hbar \mathrm{d}\boldsymbol{k}}\Delta f(\mu,\boldsymbol{k})$$

Note that this definition of the inter-band BCD in our case is different but similar to the definition of the intra-band BCD. We call the BCD in our case the inter-band BCD that integrates all available initial and final states of optical transitions. This inter-band BCD is a part of the intra-band BCD, and they become the same if only two bands (the conduction band and valence band) contribute significantly to the BCD. Both definition of the BCDs have been used in previous studies on nonlinear physical responses. For example, the intra-band BCD has been reported for the nonlinear Hall effect and the inter-band BCD has been demonstrated for the circular photogalvanic effect. Both intra-band BCD and inter-band BCD are regarded and studied as the intrinsic properties of the band structure of a material.

Before proceeding, we would like to switch from the Moiré band picture back to the WSe_2 band picture to examine the difference between inter-band and intra-band transitions (in the WSe_2 band picture). We denote the conduction and valence bands of WSe_2 as $|1, \boldsymbol{k}\rangle_0$ and $|-1, \boldsymbol{k}\rangle_0$ with a subscript 0, respectively. The Berry curvature of the WSe_2 valence band is known to be dominantly contributed by the matrix elements between the conduction and valence bands:

$$\Omega_z^{\mathrm{v}}(\boldsymbol{k}) \approx i \sum_{n \neq n'} \frac{\left\langle 1 \left| \frac{\partial H}{\partial k_x} \right| -1 \right\rangle_0 \left\langle -1 \left| \frac{\partial H}{\partial k_y} \right| 1 \right\rangle_0 - \left\langle 1 \left| \frac{\partial H}{\partial k_y} \right| -1 \right\rangle_0 \left\langle -1 \left| \frac{\partial H}{\partial k_x} \right| 1 \right\rangle_0}{[\varepsilon_1(\boldsymbol{k}) - \varepsilon_{-1}(\boldsymbol{k})]^2}$$

The Berry curvature of the conduction band has similar situation.

In terms of the WSe_2 bands, the general form of n-th Moiré band is

$$|n, \boldsymbol{k}\rangle = \sum_{m=\pm 1, \boldsymbol{G}} u_{n,\boldsymbol{G}}^{m} |m, \boldsymbol{k} + \boldsymbol{G}\rangle_0$$

where $\boldsymbol{G}$ runs over all the Moiré reciprocal lattice momenta. We note that all the states $|m, \boldsymbol{k}+\boldsymbol{G}\rangle_0$ are in the same WSe_2 valley (and we have omitted the valley index for simplicity) because the inter-valley Moiré potential is typically exponentially small. Assume the strength of the SiP Moiré potential is W (the largest $W_{\boldsymbol{Q}}$ in the Moiré $\boldsymbol{k}\cdot\boldsymbol{p}$ model in Methods), which is usually small. The largest wavefunction component $u^m_{n,\boldsymbol{G}}$ will be around 1 achieved when $m = \mathrm{sgn}(n)$ (the sign function), and $\boldsymbol{G}$ being the $|n|$-th smallest Moiré reciprocal vector (for instance, $\boldsymbol{G} = \boldsymbol{0}$ when $|n| = 1$). The second largest component $u^m_{n,\boldsymbol{G}}$ will be of order W/E_{g}, where E_{g} is the characteristic energy scale of the monolayer WSe_2 bands, here taken to be the WSe_2 band gap; these second largest components typically occur when $\boldsymbol{G}$ is the $(|n| \pm 1)$-th smallest Moiré reciprocal vector, namely, nearest reciprocal momentum neighbors of the $|n|$-th smallest Moiré reciprocal vector.

For WSe_2 inter-band optical transitions, the dominant contribution of order 1 comes from transitions from valence Moiré states $|-n, \boldsymbol{k}\rangle$ to conduction Moiré states $|n, \boldsymbol{k}\rangle$ ($n > 0$, namely, $n_{\mathrm{I}} = -n_{\mathrm{F}} = -n$), which is approximately equivalent to transitions from states $|-1, \boldsymbol{k}\rangle_0$ to $|1, \boldsymbol{k}\rangle_0$ in the WSe_2 band basis. This indicates that $V(\boldsymbol{k})$ for inter-band transitions can be approximately estimated by the Berry curvature as:

$$V(\boldsymbol{k}) \approx \frac{2e^2}{\hbar^2}|\boldsymbol{A}|^2\Omega_z^{\mathrm{v}}(\boldsymbol{k}+\boldsymbol{G})E_{\mathrm{g}}^2$$

where E_{g} is the WSe_2 band gap, $\Omega_z^{\mathrm{v}}(\boldsymbol{k})$ is the WSe_2 valence band Berry curvature, and $\boldsymbol{G}$ is the Moiré momentum, where $u^m_{n,\boldsymbol{G}}$ is the largest.

For WSe_2 intra-band optical transitions, we assume that within the valence band (as the experiment does), the transitions are restricted between valence Moiré bands, and the leading amplitude will be between Moiré states $|-n, \boldsymbol{k}\rangle$ and $|-n-1, \boldsymbol{k}\rangle$ ($n > 0$), which is of order W/E_{g}. Rewriting them

into the WSe_2 band basis, the transition coefficient $V(\boldsymbol{k})$ will contain a leading component proportional to the WSe_2 Berry curvature and order $\left(\frac{W}{E_\mathrm{g}}\right)^2$ smaller, namely:

$$V(\boldsymbol{k}) \sim \frac{2e^2}{\hbar^2}|\boldsymbol{A}|^2\Omega_z^{\mathrm{v}}(\boldsymbol{k}+\boldsymbol{G})E_\mathrm{g}^2\left(\frac{W}{E_\mathrm{g}}\right)^2 = \frac{2e^2}{\hbar^2}|\boldsymbol{A}|^2\Omega_z^{\mathrm{v}}(\boldsymbol{k}+\boldsymbol{G})W^2$$

where $\boldsymbol{G}$ is the Moiré momentum and $u_{n,\boldsymbol{G}}^m$ is the largest.

Therefore, the number of photo-excited carriers in *k*-space is approximately proportional to the value of the Berry curvature of the initial/final state, with a coefficient proportional to E_g^2 for the inter-band transition and proportional to W^2 for intra-band transition.

The total direct electrical current can be obtained by integrating all the photo-excited carriers (here, we switched from the Moiré band picture back to the WSe_2 band picture, i.e., rewriting $\boldsymbol{k}+\boldsymbol{G}$ as the WSe_2 momentum $\boldsymbol{k}$, and integrating it into the WSe_2 Brillouin zone)

$$\boldsymbol{J}_\mathrm{C} = -\frac{2\pi e\tau}{\hbar}\sum_{I,F}\int\frac{\mathrm{d}^2\boldsymbol{k}}{(2\pi)^2}\Delta\boldsymbol{v}(\boldsymbol{k})V(\boldsymbol{k})\delta[\Delta\varepsilon(\boldsymbol{k})-\hbar\omega]\Delta f(\mu,\boldsymbol{k})$$

$$\approx -\frac{8\pi\omega^2e^3\tau\Lambda}{\epsilon_0c\hbar^3}I\int\frac{\mathrm{d}^2\boldsymbol{k}}{(2\pi)^2}\frac{\mathrm{d}\big(\Delta\varepsilon(\boldsymbol{k})\big)}{\hbar\mathrm{d}\boldsymbol{k}}\Omega_z^{\mathrm{v}}(\boldsymbol{k})\Delta f(\mu,\boldsymbol{k})\delta[\Delta\varepsilon(\boldsymbol{k})-\hbar\omega]$$

$$\sim \frac{8\pi\omega^2e^3\tau E_\mathrm{g}\Lambda}{\epsilon_0c\hbar^3}I\int\frac{\mathrm{d}^2k}{(2\pi)^2}\frac{\mathrm{d}\Omega_z^{\mathrm{v}}(\boldsymbol{k})}{\hbar\mathrm{d}\boldsymbol{k}}\Delta f(\mu,\boldsymbol{k})\delta[\Delta\varepsilon(\boldsymbol{k})-\hbar\omega]$$

where $I=\epsilon_0c|\boldsymbol{A}|^2/2\omega^2$ is the light intensity, the coefficient $\Lambda=E_\mathrm{g}^2$ for inter-band transition, and $\Lambda=W^2$ for intra-band transition. For the intra-band transition within the valence band, one can approximate $\Delta f(\mu,\boldsymbol{k})$ as 1 for $\boldsymbol{k}$ in the hole pocket and as 0 for $\boldsymbol{k}$ outside the hole pocket.

16. Valley imbalance of the intra-band transition at the WSe_2/SiP hetero-interface

To understand the optical transitions within the valence band of monolayer WSe_2, we discussed the atomic wavefunctions and the resultant optical selection rule therein. The atomic wavefunctions of transition metal dichalcogenides of the conduction and valence bands are known to be dominated by the *d* orbitals of the transition metals, in which (in the absence of Moiré potential) the wavefunctions of the conduction band are formed by $\left|\Psi_{\mathrm{c}}^{\pm \mathrm{K},s}\right\rangle = |d_{z^2}\rangle|s\rangle$ and the wavefunctions of the valence band are formed by $\left|\Psi_{\mathrm{v}}^{\pm \mathrm{K},s}\right\rangle = \frac{1}{\sqrt{2}}\left(\left|d_{x^2-y^2}\right\rangle \pm i\left|d_{xy}\right\rangle\right)|s\rangle$ with $|s\rangle$ for spin up $|\uparrow\rangle$ and spin down $|\downarrow\rangle$ states. We also note that the above *d* orbitals associated with the conduction and valence bands are only accurate at the K and −K points. Away from the K and −K points, the valence band also gains a component of $|d_{z^2}\rangle$, and similarly the conduction band also gains a component of $\frac{1}{\sqrt{2}}\left(\left|d_{x^2-y^2}\right\rangle \pm i\left|d_{xy}\right\rangle\right)$. Since the orbital angular momenta of the conduction band and the valence band are found to be $l = 0$ and $l = \pm 2$, respectively, and the spin angular momentum is $s = \pm\frac{1}{2}$, the electronic states of the conduction bands and valence bands can be labeled by the total angular momenta $m = l + s$ as follows:

$\left|\Psi_{\mathrm{c}}^{\mathrm{K},\uparrow}\right\rangle = \left|m = \frac{1}{2}\right\rangle$, $\left|\Psi_{\mathrm{c}}^{\mathrm{K},\downarrow}\right\rangle = \left|m = -\frac{1}{2}\right\rangle$, $\left|\Psi_{\mathrm{c}}^{-\mathrm{K},\uparrow}\right\rangle = \left|m = \frac{1}{2}\right\rangle$, $\left|\Psi_{\mathrm{c}}^{-\mathrm{K},\downarrow}\right\rangle = \left|m = -\frac{1}{2}\right\rangle$, $\left|\Psi_{\mathrm{v}}^{\mathrm{K},\uparrow}\right\rangle = \left|m = \frac{5}{2}\right\rangle$, $\left|\Psi_{\mathrm{v}}^{\mathrm{K},\downarrow}\right\rangle = \left|m = \frac{3}{2}\right\rangle$, $\left|\Psi_{\mathrm{v}}^{-\mathrm{K},\uparrow}\right\rangle = \left|m = -\frac{3}{2}\right\rangle$, $\left|\Psi_{\mathrm{v}}^{-\mathrm{K},\downarrow}\right\rangle = \left|m = -\frac{5}{2}\right\rangle$.

Since the photon carries an angular momentum of 1 (or −1) with right-handed (or left-handed) circularly-polarized light σ^+ (or σ^-), the optical transition should satisfy a conservation law of the angular momentum. As a result, the total angular momentum of the final state and that of the initial state defers 1 (or −1) of angular momentum in the optical transition process excited by right-handed (or left-handed) circularly-polarized light σ^+ (or σ^-). Note that such the conservation law of the

angular momentum should be understood in a manner with a module of 3 due to the phase winding of the Bloch states with the three-fold rotational symmetry of transition metal dichalcogenides.

For the K valley, the direct inter-band optical transition occurs from the initial state at the valence band maximum of the $|n_{\mathrm{I}}\rangle = \left|\Psi_{\mathrm{v}}^{\mathrm{K},\uparrow}\right\rangle$ state, whose total angular momentum is $m = \frac{5}{2}$. With excited right-handed circularly-polarized light σ^+, the final state is $|n_F\rangle = \left|m = \frac{7}{2}\right\rangle$, whose total angular momentum is equivalent to $m = \frac{1}{2}$ by modulo 3. Therefore, the final state of the optical transition is $\left|m = \frac{1}{2}\right\rangle = \left|\Psi_{\mathrm{c}}^{\mathrm{K},\uparrow}\right\rangle$. For simplification, we denote this optical transition process as $\left|\Psi_{\mathrm{v}}^{\mathrm{K},\uparrow}\right\rangle \xrightarrow{\sigma^+} \left|\Psi_{\mathrm{c}}^{\mathrm{K},\uparrow}\right\rangle$. In sharp contrast, all three other optical transition processes of $\left|\Psi_{\mathrm{v}}^{\mathrm{K},\uparrow}\right\rangle \xrightarrow{\sigma^+} \left|\Psi_{\mathrm{c}}^{\mathrm{K},\downarrow}\right\rangle$, $\left|\Psi_{\mathrm{v}}^{\mathrm{K},\uparrow}\right\rangle \xrightarrow{\sigma^-} \left|\Psi_{\mathrm{c}}^{\mathrm{K},\downarrow}\right\rangle$ and $\left|\Psi_{\mathrm{v}}^{\mathrm{K},\uparrow}\right\rangle \xrightarrow{\sigma^-} \left|\Psi_{\mathrm{c}}^{\mathrm{K},\uparrow}\right\rangle$ are impossible and completely prohibited by the conservation law of the angular momentum. As a result, the inter-band optical transition at the K valley is fully circularly-polarized by σ^+. Similar to the above analysis, the inter-band optical transition at the −K valley is fully circularly-polarized by σ^-, and therefore, the inter-band optical transition is valley selective.

To understand the details of the intra-band optical transition of the heterointerface, we count the angular momenta of all valence band states of monolayer WSe_2 and analyze the possibility of each optical transition process. Since the Moiré potential caused by the bottom SiP generates the Moiré reciprocal momenta, as mentioned before, the direct optical transition between the Moiré bands of the heterointerface, in some sense, can be understood as the indirect intra-band optical transition of monolayer WSe_2. Importantly, the Moiré potential hybridizes the $\frac{1}{\sqrt{2}}\left(\left|d_{x^2-y^2}\right\rangle \pm i\left|d_{xy}\right\rangle\right)$ and $|d_{z^2}\rangle$ orbitals of conduction and valence bands (the same spin to the lowest order) in the same valley of monolayer WSe_2, thus hybridizing their angular momenta. In addition, states within the valence band at different momenta can also carry different angular momenta. Therefore, for instance, a valence

Moiré eigenstate in valley K will be of the form $c_1\left|\Psi_{+2}^{\mathrm{K},\uparrow}\right\rangle + c_2\left|\Psi_{0}^{\mathrm{K},\uparrow}\right\rangle$, where the coefficients $|c_2|/|c_1| \sim W/E_{\mathrm{g}}$, and the states $\left|\Psi_{+2}^{\mathrm{K},\uparrow}\right\rangle$ and $\left|\Psi_{0}^{\mathrm{K},\uparrow}\right\rangle$ stand for the components of orbitals $\frac{1}{\sqrt{2}}\left(\left|d_{x^2-y^2}\right\rangle + i\left|d_{xy}\right\rangle\right)$ and $|d_{z^2}\rangle$, respectively (represented by angular momentum subindices $l = +2,0$). In particular, $\left|\Psi_{+2}^{\mathrm{K},\uparrow}\right\rangle$ is dominated by $\left|\Psi_{\mathrm{v}}^{\mathrm{K},\uparrow}\right\rangle$ at the K point, while $\left|\Psi_{0}^{\mathrm{K},\uparrow}\right\rangle$ is contributed by both $\left|\Psi_{\mathrm{c}}^{\mathrm{K},\uparrow}\right\rangle$ and $\left|\Psi_{\mathrm{v}}^{\mathrm{K},\uparrow}\right\rangle$ with moire momenta $\boldsymbol{G}$ away from the K point, where $\left|\Psi_{\mathrm{c,v}}^{\mathrm{K},\uparrow}\right\rangle$ are the WSe_2 eigenstates before the Moiré potential is added. Therefore, the intra-band transition process between two valence Moiré eigenstates will be of the form $|n_{\mathrm{I}}\rangle = c_1\left|\Psi_{+2}^{\mathrm{K},\uparrow}\right\rangle + c_2\left|\Psi_{0}^{\mathrm{K},\uparrow}\right\rangle \rightarrow |n_{\mathrm{F}}\rangle = c_1'\left|\Psi_{+2}^{\mathrm{K},\uparrow}\right\rangle + c_2'\left|\Psi_{0}^{\mathrm{K},\uparrow}\right\rangle$. According to our discussion of angular momentum of the basis $\left|\Psi_{\mathrm{c,v}}^{\mathrm{K},\uparrow}\right\rangle$ above, the intra-band transition probability of σ^+ (σ^-) polarized light at valley K is proportional to $\left|c_2'^{*}c_1\right|^2$ ($\left|c_1'^{*}c_2\right|^2$). The transition probabilities of σ^+ and σ^- polarization at valley $-K$ are exchanged, as ensured by the time-reversal symmetry. In general, $\left|c_2'^{*}c_1\right|^2 \neq \left|c_1'^{*}c_2\right|^2$, so the intra-band optical transition is valley imbalanced. If $|n_{\mathrm{I}}\rangle$ is away from the K point and $|n_{\mathrm{F}}\rangle$ is near the K point, then $|c_2'|/|c_1'| \ll |c_2|/|c_1|$ (since $W/E_{\mathrm{g}} \ll 1$), and the intra-band transition at the K valley will dominantly select the σ^- polarized light.

We note that the inter-valley optical transition is forbidden, since the two valleys differ by a momentum much larger than the primitive Moiré lattice momentum and do not satisfy the momentum conservation even with the Moiré potential (more strictly speaking, this transition is only possible at very high order of perturbation and is thus exponentially suppressed).